



Article

Analyzing Archive Transit Multibeam Data for Nodule Occurrences

Mark E. Mussett ^{1,2} , David F. Naar ^{1,*}, David W. Caress ³ , Tracey A. Conrad ², Alastair G. C. Graham ⁴,
Max Kaufmann ² and Marcia Maia ⁵

¹ College of Marine Science, University of South Florida, Tampa, FL 33620, USA; markmussett@usf.edu

² Odyssey Marine Exploration, Tampa, FL 33609, USA; markm@odysseymarine.com (M.E.M.);
tconrad@odysseymarine.com (T.A.C.); mkaufmann@odysseymarine.com (M.K.)

³ Monterey Bay Aquarium Research Institute, Moss Landing, CA 95039, USA; caress@mbari.org

⁴ School of Earth and Environmental Sciences, Cardiff University, Cardiff CF10 3AT, UK; graham15@cardiff.ac.uk

⁵ Geo-Ocean, UMR 6538 CNRS-IFREMER-UBO-UBS, 29280 Plouzané, France; marcia.maia@univ-brest.fr

* Correspondence: naar@usf.edu

Abstract: We show that analyzing archived and future multibeam backscatter and bathymetry data, in tandem with regional environmental parameters, can help to identify polymetallic nodule fields in the world's oceans. Extensive archived multibeam transit data through remote areas of the world's oceans are available for data mining. New multibeam data will be made available through the Seabed 2030 Project. Uniformity of along- and across-track backscatter, backscatter intensity, angular response, water depth, nearby ground-truth data, local slope, sedimentation rate, and seafloor age provide thresholds for discriminating areas that are permissive to nodule presence. A case study of this methodology is presented, using archived multibeam data from a remote section of the South Pacific along the Foundation Seamounts between the Selkirk paleomicroplate and East Pacific Rise, that were collected during the 1997 Foundation–Hotline expedition on R/V *Atalante*. The 12 kHz Simrad EM12D multibeam data and the other forementioned data strongly suggest that a previously unknown nodule occurrence exists along the expedition transit. We also compare the utility of three different backscatter products to demonstrate that scans of printed backscatter maps can be a useful substitute for digital backscatter mosaics calculated using primary multibeam data files. We show that this expeditious analysis of legacy multibeam data could characterize benthic habitat types efficiently in remote deep-ocean areas, prior to more time-consuming and expensive video and sample acquisition surveys. Additionally, utilizing software other than specialty sonar processing programs during this research allows an exploration of how multibeam data products could be interrogated by a broader range of scientists and data users. Future mapping, video, and sampling cruises in this area would test our prediction and investigate how far it might extend to the north and south.

Keywords: multibeam echosounder; backscatter; polymetallic nodules; benthic habitat mapping; angular response



Citation: Mussett, M.E.; Naar, D.F.; Caress, D.W.; Conrad, T.A.; Graham, A.G.C.; Kaufmann, M.; Maia, M. Analyzing Archive Transit Multibeam Data for Nodule Occurrences. *J. Mar. Sci. Eng.* **2024**, *12*, 2322. <https://doi.org/10.3390/jmse12122322>

Academic Editor: Chun-Feng Li

Received: 28 October 2024

Revised: 25 November 2024

Accepted: 10 December 2024

Published: 18 December 2024



Copyright: © 2024 by the authors. Licensee MDPI, Basel, Switzerland. This article is an open access article distributed under the terms and conditions of the Creative Commons Attribution (CC BY) license (<https://creativecommons.org/licenses/by/4.0/>).

1. Introduction

Polymetallic nodules, also known as manganese nodules or ferromanganese (Fe-Mn) nodules, grow out of seawater or sediment pore water around any hard nucleus on deep-sea sediments, and exist at various locations throughout the global ocean [1–5]. Individual nodules can range from <1 to 20 cm, with most measuring 1–12 cm, and fields can cover hundreds of km² with highly variable abundance [1,5–7]. Nodules serve as a deep-sea benthic habitat, and are of economic interest owing to their metal content, as they are often enriched in Mn, Fe, Ni, Cu, Co, Ti, and rare earth elements [1,3,5,8–23].

Existing analytical methods to identify prospective nodule areas include a review of oceanographic, geographic, geologic, and environmental parameters, supplemented with a review of existing geological samples and seafloor photography records [14,24–37].

Principal component analysis of sediment characteristics can be incorporated with inputs for environmental values to facilitate mineral prospectivity mapping [26,38]. Mizell et al. (2022) note that areas conducive to nodule occurrence generally exhibit low bathymetric relief, low-to-moderate sedimentation rate and surface productivity, water depths near or below the carbonate compensation depth, and pre-Quaternary crustal age, which typically implies that the seafloor has subsided sufficiently to be below the CCD (carbonate compensation depth), and adequate time has passed for accretion of a nodule around a nucleus [34]. Nodule occurrences may not be contiguous within an area, and often exhibit variable abundance and predominate physical characteristics, e.g., in their size and shape [39].

Acoustic backscatter data can aid in identifying nodules on the seafloor [9,11,18,40–46]. Oceanographic remote sensing data, including multibeam bathymetry and backscatter data, can be used to analyze prospective areas identified through initial desktop research. Previously collected, archived multibeam data are readily available for research, and additional multibeam data can be collected during follow-up site investigations. However, the utility of multibeam data collected during full speed transits for identifying nodule occurrence is not often considered or discussed in the literature. Normally, exploratory surveys are planned with managed speed, sensor settings, regular sound velocity profile collection, etc., and may be undertaken with hull-mounted, towed, or AUV-mounted multibeam and side-scan systems [2,6,11,46–67].

The methodology described in this research is novel in that it further explores the use of transit multibeam backscatter and bathymetry for identifying potential nodule presence, with subsequent analysis of environmental parameters to evaluate whether the geographic context supports nodule formation, following the initial (Master's thesis) work by Mussett (2023) [68]. This research also investigates the use of angular response analysis to further classify the seafloor geology in the study area and to compare to our direct interpretation of backscatter raster data [6,46,69–73]. Processed multibeam backscatter data are normalized to a specific angle or range of angles from the multibeam data, whereas angular response diagrams preserve backscatter value as a function of incidence angle [74,75]. The relationship of across-track backscatter with incidence angle can aid in identifying the specific substrate type [76]. Differences in seafloor geology result in different backscatter intensities at a given incidence angle or grazing angle [70,74,75,77–81]. While backscatter strength can be relied upon as an interpretive basis for less or more absorptive seafloor lithology, e.g., clay versus lava, angular response analysis can complement interpretations of two areas exhibiting similar strength. For instance, if two surveyed expanses of seafloor both exhibit similarly low backscatter values, suggestive of acoustically absorptive sediment, the profiles of their respective angular response diagrams can aid in discerning similarities or differences in sediment type (in terms of grain size) between the areas [72,76].

A comparison between the results from the backscatter raster data analysis and the (state-of-the-art) angular response analysis is made in the discussion section. Note also that the angular response diagram generation undertaken in this research is based on pixel-value backscatter raster data. This provides an alternative to multibeam processing software methods for angular response analysis, as it requires only a backscatter raster product, and provides analysis based on averaged along-track pixel values, rather than from a per-ping acoustic data file.

This case study uses Simrad EM12D (12 kHz) multibeam data collected during the Foundation–Hotline expedition aboard R/V *Atalante*, operated by IFREMER between Papeete (Tahiti) and Easter Island (Chile) in January and February 1997. The primary objectives of the cruise were to map and date the Foundation Seamount chain up to the East Pacific Rise (EPR) [82,83], but here we focus on the data collected during the transit between the Selkirk paleomicroplate and the Foundation Seamounts (Figure 1).

The data coverage area includes an approximately 125 km long swath of homogenous high backscatter, hereafter referred to as Area A (Figure 1). Area A predominately consists of low-relief seafloor, and is distal from any known recent lava flows from any nearby seafloor spreading systems or submarine volcanoes. This study analyzes multibeam

bathymetry and backscatter data, auxiliary data regarding geographic parameters, and angular response of the backscatter, in order to investigate if the high backscatter data in this area could be due to a large, previously uncharted and unexplored nodule field.

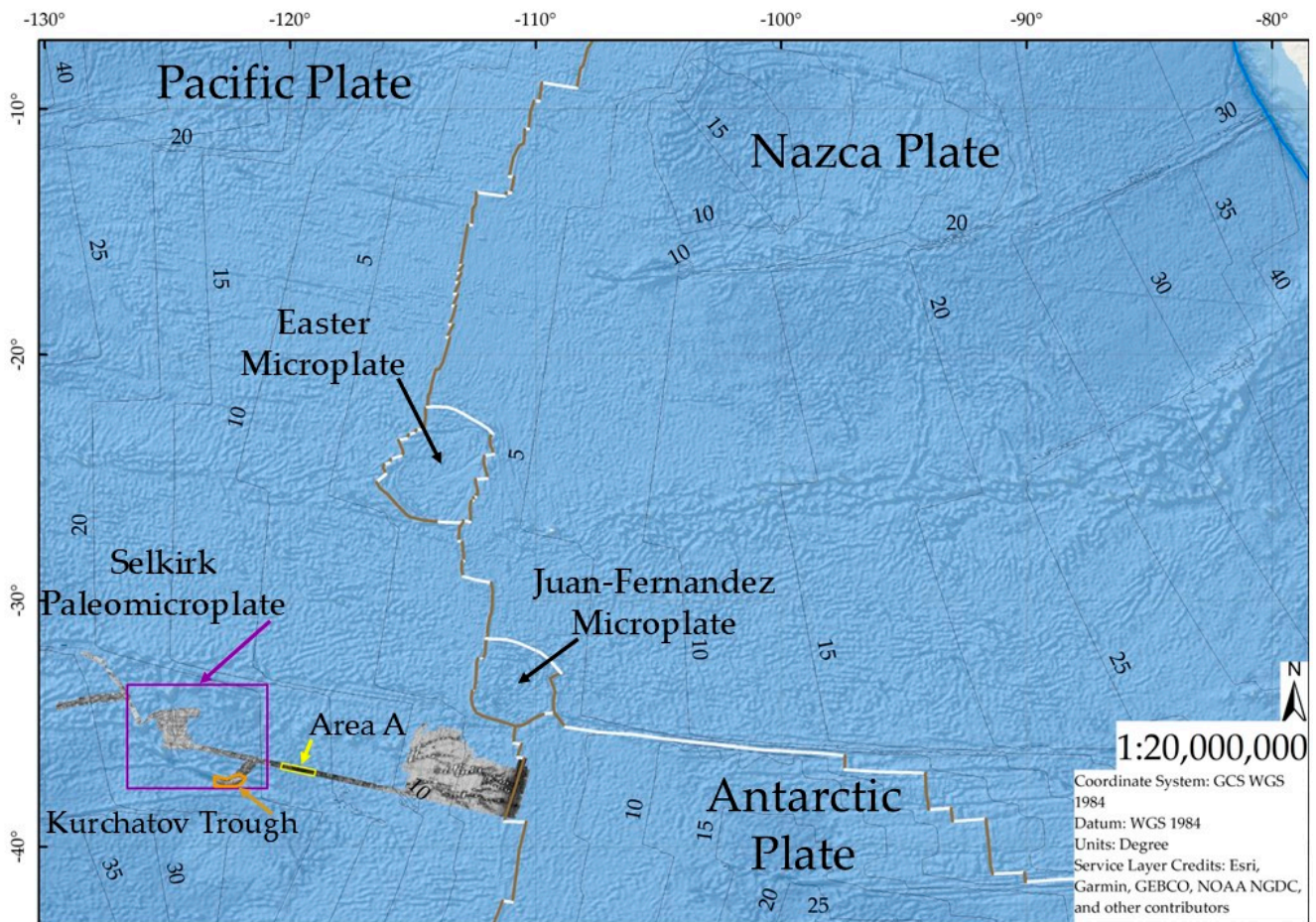


Figure 1. Regional context. The grayscale shading indicates the case study data area. Tectonic plate boundaries are shown, with blue lines indicating convergent boundaries, white lines indicating transform boundaries, and brown lines indicating divergent boundaries [84]. Seafloor age is shown by black isochrons in 5 Ma intervals, adapted from [85]. Tectonic plates are labeled, with the Selkirk paleomicroplate highlighted in purple; Area A is highlighted in yellow, and the Kurchatov trough is highlighted in orange [86].

2. Observations

2.1. Transit Observations and Geological Setting

The ship transit investigated in this study trends approximately 102° , and spans from approximately -32° latitude, -130° longitude to -39° latitude, -110° longitude. The transit crosses the Pacific plate from about ~ 25 Ma, across the EPR at 0 Ma, and out to ~ 1 Ma onto the Antarctic plate [84,85], and crosses a variety of seafloor terrain, including abyssal hills, submarine volcanoes, lava flows, sedimented seafloor, and tectonic fabric and structures related to the Selkirk paleomicroplate (>20 Ma) in the far west [86].

Area A is not documented in the literature as a known occurrence or a region that is highly permissive to nodule formation [7,13,14,24,26,27,30–37,87–89], and it is ~ 115 km north of suggested areas of low nodule abundance [26,88] and ~ 1700 km east from suggested areas of high abundance [34]. However, there are two proximal ground-truth sites that indicate nodules. One site (-36.33° latitude, -121.50° longitude) is <2 km from the northern extent of the data set and ~ 100 km to the northwest of Area A. This site provided a nodule sample recovered during sediment coring during the 14th cruise of R/V Dmitry

Mendelev in 1975 [90]. The other site, from -35.22° latitude, -124.97° longitude within the data set, and ~ 450 km west of Area A, consists of seafloor photos collected at core station 16, visited during the 24th cruise of USNS Eltanin in 1966. The core description indicates 2–5% micronodules in the upper 7 cm of core [91]. Seafloor photos from the station indicate abundant nodule coverage [68,92].

Water depths in the data set range from 334 m (seamount summits) to 6630 m (failed rifts, trenches, fracture zones or pseudofaults related to the Selkirk paleomicroplate) [86]; the average seafloor depths from west to east along the transit (apart from the aforementioned shallow and deep features) rise from below to above the CCD, and are regionally estimated at approximately 4100 m [93].

2.2. Environmental Parameters Suitable for Nodule Formation

This research considers water depth relative to the CCD, seafloor slope, sedimentation rate, and seafloor age as environmental parameters impacting the suitability for the seafloor to contain a nodule occurrence, as described below. These parameters are applied on a cutoff basis, so that if a specific seafloor site does not meet these parameter thresholds, potential nodule presence is ruled out. Likewise, these parameters are not applied in this research as a basis for calculating specific nodule abundance, but rather only the potential for nodule occurrence. Additionally, the authors acknowledge that nodules can exist at locations where these parameters are not wholly met. However, taken as an aggregated set of conditions, and combined with backscatter data analysis, these conditions serve as guidelines for determining whether nodules may exist at a given location on a first-order basis.

A seafloor below or near the CCD is considered a suitable environment for nodule formation [1,3,4,7,14,16,27]. Some nodule fields do exist above the CCD, e.g., the Blake Plateau [4,94–96], the Galicia Bank [97], the Pernambuco Plateau [98], and the South China Sea [99], and these have different environmental constraints, which should be further reviewed to identify additional parameters that control their occurrence, such as the limitation of sedimentation resulting from strong near-bottom currents. This study focuses on nodule occurrence in deep water only.

The slope of the seafloor is also an important parameter for determining nodule presence from multibeam backscatter data. Areas delineated from hull-mounted, deep-water multibeam data as exhibiting a seafloor slope $\leq 7^\circ$ can be considered conducive to nodule existence, and low-slope environments, e.g., $<10^\circ$, further limit the impact of slope on acoustic backscatter [17,41].

Additionally, a very low sedimentation rate of 0.3 to <1 cm ka^{-1} is considered coincident with nodule presence [1,13,24,100,101]. The sedimentation rate can be estimated using surface productivity as a proxy of POC (particulate organic carbon) flux to the seafloor [102,103], or by dividing sediment thickness [104] by seafloor age [85].

Seafloor age can also dictate whether an area is permissive to nodule occurrence. Newly created seafloor is often shallower than the local CCD, as is the case for the EPR and associated ridge structures included in this case study's data. Additionally, time is required for newly created seafloor to subside to water depths below the CCD. Also, if an area is over a recent lava flow, adequate time may not have lapsed for nodule accretion atop newly sedimented seafloor. Likewise, considering an estimated hydrogenetic radial nodule growth rate of 5 mm Ma^{-1} [1] to ~ 7 mm Ma^{-1} [90], a minimum of 2 Ma growth time is necessary for an accretion to reach a minimum 2 cm diameter, irrespective of nucleus size or mineral replacement of the nucleus. Hence, a 2 Ma minimum age can be considered a requirement for nodule formation where a slow growth rate exists.

The influence of bottom water, dissolved oxygen concentrations in seawater, available sources of nuclei, dissolved metal content, and microtopography are not considered in this study, owing to a lack of data for this case study, and a lack of agreement on the influence of these parameters on abundant nodule presence.

2.3. Transit Areas Aligning with Prospective Nodule Characteristics

Along the transit near the EPR, all areas younger than 12 Ma are shallower than 4000 m, and are therefore above the estimated shallowest threshold for nodule presence, considering a local CCD depth of ~4100 m [93] as the general ceiling for nodule occurrence in the Pacific [1,3,9]. Therefore, the youngest areas are neither old enough nor deep enough to satisfy the requisite characteristics for nodule prospectivity. Most areas of older seafloor within the transit, including Area A, are not much deeper than 4000 m, except for the Kurchatov trough and the low slope seafloor immediately to its south.

The entirety of the data set (except very near the EPR) exhibits a sedimentation rate <1 (cm ka^{-1}) [85,104], therefore meeting the requisite sedimentation threshold described above.

Much of the data exhibit slopes less than the maximum threshold of 7° for nodule presence, though the areas near the EPR and off-axis volcanic seamount chains, the tectonic structures of the Kurchatov trough and the Selkirk paleomicroplate, and the isolated abyssal hill feature exhibit slopes greater than 7° . Both Area A and the area south of the Kurchatov trough consist of low-slope seafloor, along- and across-track. Areas within the data where these conditions are met are indicated below (Figure 2).

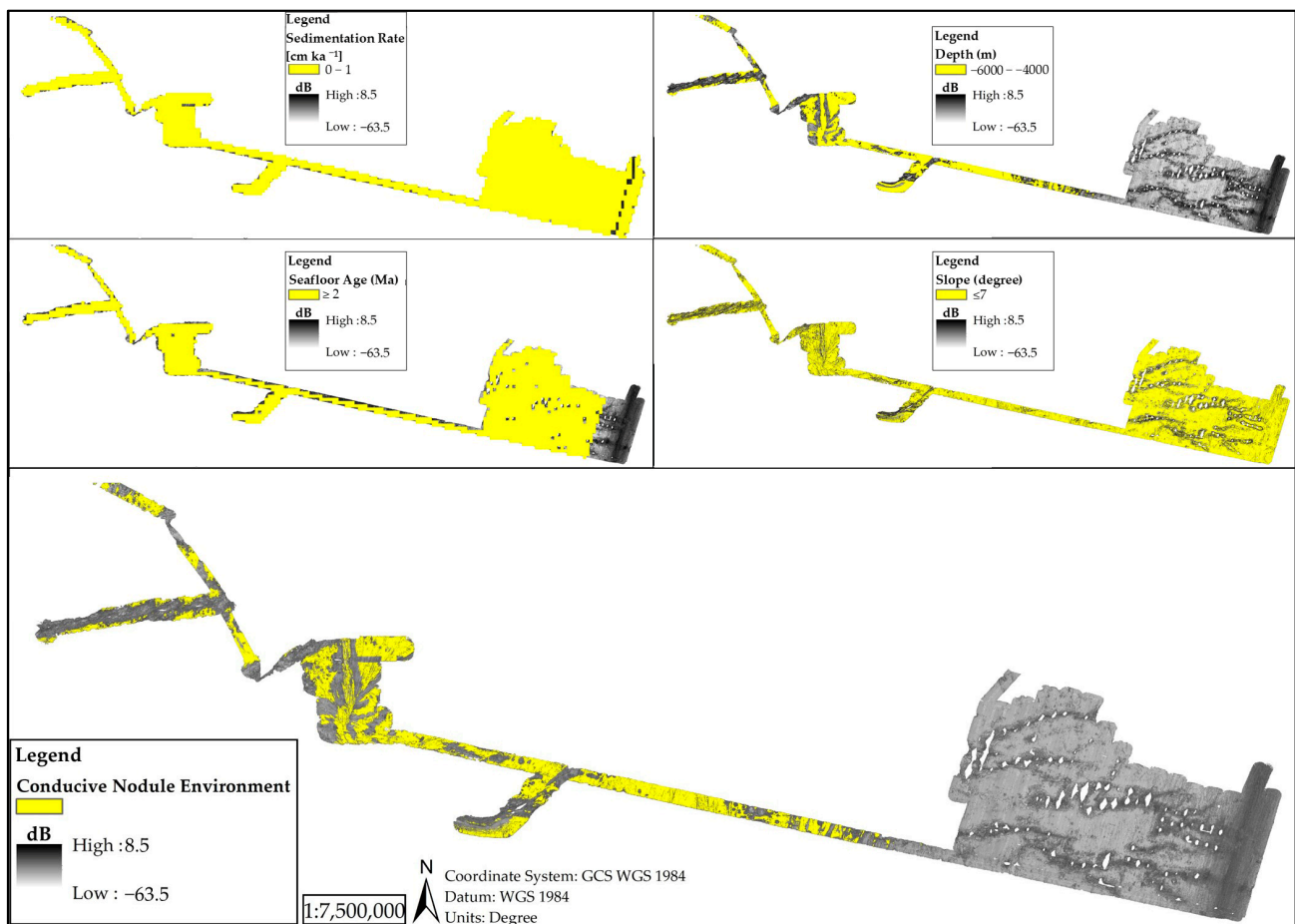


Figure 2. Environmental parameter limits. The top 4 panels show their respective parameters. The bottom panel shows the area within the data where all parameters are met. This area is taken to be conducive to nodule occurrence.

3. Research Objectives

This research will attempt to predict whether a previously undescribed nodule occurrence exists within the data area, and whether it may relate to a larger nodule occurrence in the region. Methods will explore the utility of transit multibeam backscatter, firstly, and bathymetry, secondly, for identifying potential nodule presence. Likewise, this research

will address the suitability of backscatter products, rather than raw multibeam data, for identifying nodule presence on the deep seafloor. This will be carried out by comparing results from the analysis of different outputs from the same original data set, e.g., 8-bit visualization of backscatter, a surface containing backscatter intensity values. This assessment will also inform whether the differing backscatter products produced from the same data, but with different software or methods, can provide similar interpretations of seafloor characterization. Angular response diagrams from different visually apparent domains within the data will provide an additional basis against which to verify characterizations based on backscatter value, bathymetry, and geologic parameters.

4. Materials and Methods

4.1. 8-Bit Graphic Paper Chart Analysis

Paper charts displaying the backscatter as 8-bit grayscale images were generated in real time during the expedition. These legacy maps were digitally photographed at 300 dpi resolution using a Nikon D800. The images were merged into a single digital image with 8-bit pixel values using Adobe Photoshop 2022. This digital image was georeferenced using ESRI ArcMap 10.8, yielding an 8-bit surface of 230 m × 230 m cell size [68,83]. As gain was not adjusted during data collection (coauthor D.F. Naar, personal communication, 2021) [105], and visual observation of the paper charts does not indicate apparent along-track jumps in backscatter intensity, the relative backscatter values, depicted by pixel values, were used for analysis in [68].

The visual identification of seafloor domains in these images served as the first iteration of analysis. Observation identified areas of high, low, and variable backscatter. One homogenous area overlay the EPR, which is an area of known seafloor creation, and thus its pixel characteristics could be inferred to represent high backscatter values. Areas of homogenous, high backscatter values included the EPR, volcanic and abyssal hill structures extending distally from the EPR, and Area A. The Kurchatov trough and immediately adjacent areas exhibited variable backscatter.

Histogram equalization through a cumulative distribution function, and subsequent reclassification of the backscatter into a surface of 8 bins, were undertaken as described in Mussett (2023) [68]. The reclassified backscatter data were then constrained by parameters conducive to nodule formation. This included the elimination of pixels meeting the following parameters: <50% of the maximum backscatter value, shallower than the local CCD, slope > 7°, seafloor younger than 2 Ma, and sedimentation rate $\geq 1 \text{ cm ka}^{-1}$. This methodology identified areas within the data where nodules could be present.

4.2. Comparing 8-Bit Graphic Paper Chart with Digital Backscatter Products

The EM12D data archived by IFREMER were reprocessed using MB-System version 5.8.1, <http://www.mbari.org/data/mbsystem> (accessed on 9 December 2024), distribution available at <https://github.com/dwcaress/MB-System/releases/tag/5.8.1> (accessed on 9 December 2024) [106,107], an open-source software package for processing seafloor mapping data. The bathymetry were gridded to produce a digital terrain model with 150 m resolution, and the backscatter values were mosaiced at the same resolution without any correction. The EM12D sonar produced a single log-scaled backscatter value associated with each sounding, with an 8-bit dynamic range; the values ranged from -63.5 dB to $+8.5 \text{ dB}$. In addition, the float-valued backscatter mosaic was mapped via a linear colormap to a grayscale image, with high amplitudes represented by dark shading, and low amplitudes represented by light shading. These two surfaces and the 8-bit graphic paper chart (Scan) described above are hereinafter referred to as the 'three surfaces'. The three surfaces were compared using zonal statistics.

A 90 × 90 km fishnet grid was applied to delineate zones for general visualization of the data from the three surfaces. Trendlines of standard deviation, median, and mean for the three surfaces were created to illustrate the similarities and differences between the three surfaces. Separately, a 4 × 4 km fishnet was applied to delineate zones so as

to constrain the three surfaces to their nodule-conducive area, based on bathymetry and geologic parameters. This included constraining the data to $\geq 1\sigma$ backscatter value to eliminate low backscatter zones, and further constraining the data to $\leq -1\sigma$ standard deviation to eliminate high variability zones. These constraints emphasize areas where nodules may be present based on backscatter.

The final method for zonal statistical analysis included dividing the data coverage area into longitudinally equal zones of 1° . This segmented the data into 20 zones. The number of 4×4 km cells in each zone exhibiting low backscatter variability and a high backscatter value were counted for each of the three surfaces, to identify zones with a higher concentration of prospective nodule area. The 1° zones were then constrained by bathymetric and geologic parameters to include only areas with environmental conditions conducive to nodule presence. This constraint reduced the number of 1° zones from 20 to 14. The 1° zones with the highest concentration of 4×4 km cells, following the applied constraints described above, were identified as clusters where nodules may exist. Comparisons were conducted to test the similarity of the results derived from the different methods of displaying and analyzing backscatter data.

4.3. Comparing Angular Response

Angular response diagrams were generated from select sites representing visually different backscatter domains and different geographic locations. The diagrams were derived from the cell values of the backscatter surface, with pixel values in dB, and were not taken per-ping. The nadir position was estimated from the nadir artifact position in the backscatter, and the angle was estimated as a function of water depth, swath width, and across-track pixel position relative to the nadir. The average backscatter value and diagram shape, in terms of average departure from trendline intercept, were recorded, and the qualitative profile shape was noted. These results were graphed against 15 kHz angular response backscatter data for a variety of substrate types, as described in the High-Frequency Ocean Environmental Acoustic Models Handbook, hereinafter the 'handbook' [76]. A qualitative comparison of the angular response from the test case data, and the 12 kHz angular response from a survey area described by Yang et al. (2020), was also graphed [46]. The angular response data serve as another verification for the use of backscatter data in delineating seafloor geology domains, and both the profile shape and the across-track values relative to highest near-nadir values provide a basis for comparison with theoretical profile shapes attributable to different seafloor substrates.

5. Results

The three surfaces exhibited similar trends in their 90×90 km zonal statistics, indicating that all three should generate similar results from a given analysis (Figure 3).

Producing zonal statistics for all three surfaces on a 4×4 km zonal basis (normalizing resolution to 16 km^2 cells, hereinafter 'cells') allowed for a cluster analysis to be undertaken, and for the surfaces to be compared. This was achieved by further binning the surfaces to bins of 1° longitude width (Figure 4). Constraining the three surfaces to only those cells exhibiting high backscatter values identified areas of low seafloor acoustic absorption, e.g., hard substrate including crusts, nodules, exposed basalt, etc.; additionally, constraining the surfaces to include only cells with low backscatter standard deviation (σ) further identified areas of homogenous backscatter intensity. When an area was shown to exhibit high backscatter values and high backscatter homogeneity, it was inferred as a uniform or semi-uniform expanse of relatively hard seafloor substrate.

Counting the percentage of total cells present in each 1° bin for each respective surface emphasizes clusters of strong, homogenous backscatter. This also allows for differences between the three surfaces to be examined. The results for all three surfaces are similar, with the 1° zones 8, corresponding to the Kurchatov trough area, 11, corresponding to Area A, and 19 and 20, corresponding to the EPR, emphasized as clusters of high, homogeneous backscatter (Figures 5–7; Table 1). However, while the two surfaces created from the digital

backscatter data align very closely ($R = 0.998$), the scanned surface correlates well but not as closely ($R = 0.912$), exhibiting higher stack line peaks for clusters in Zones 10, 11 and 12 (Area A and adjacent), and a lower peak in Zone 8 (Kurchatov trough).

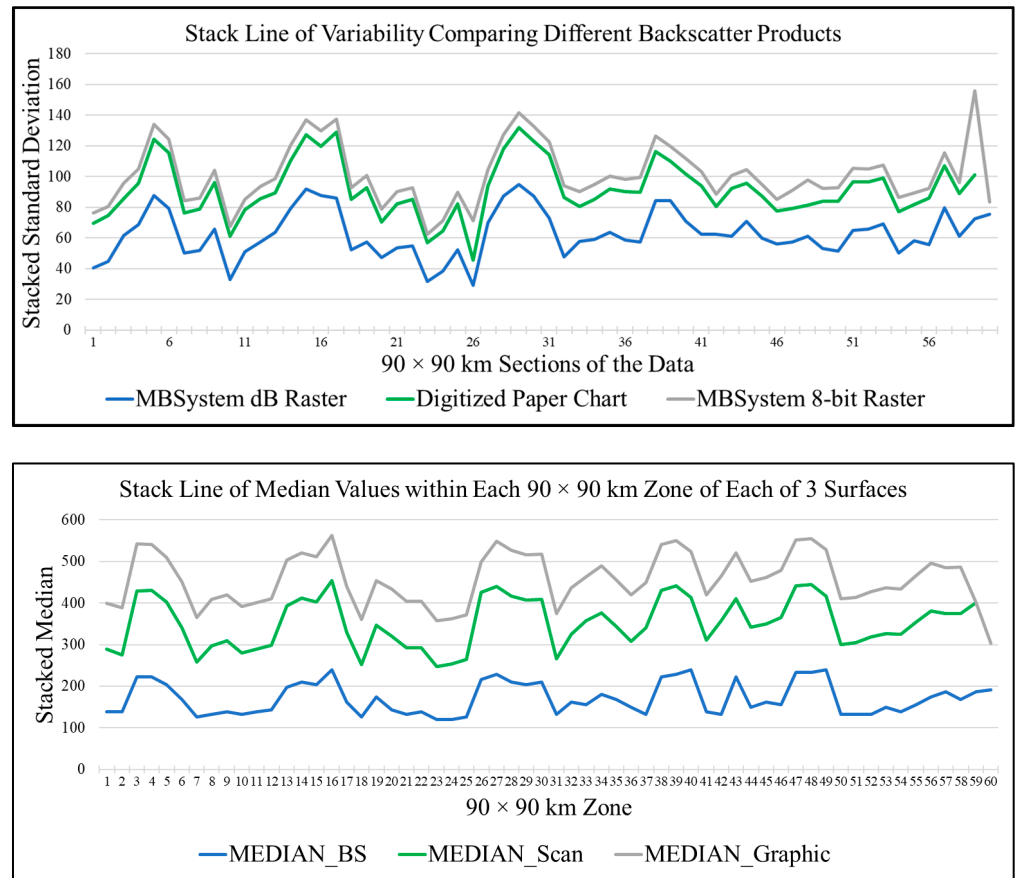


Figure 3. Stack line comparisons of the three surfaces, showing zonal statistics for median and standard deviation based on 60 zones of 90×90 km. The backscatter mosaic in dB is shown in blue, the backscatter 8-bit image is shown in gray, and the scanned paper plot of the backscatter digitized in 8-bit is shown in green. The top panel shows zonal statistics for standard deviation as an indicator of zonal homogeneity. The bottom panel shows zonal statistics for median backscatter values; note that the median backscatter values for the 'MEDIAN_BS' surface have been normalized from the dB value to 8-bit values, for comparison with 8-bit surfaces. The stack line trends show that all three surfaces share similar zonal statistics at this resolution, indicating that all three surfaces may work comparably for analyses.

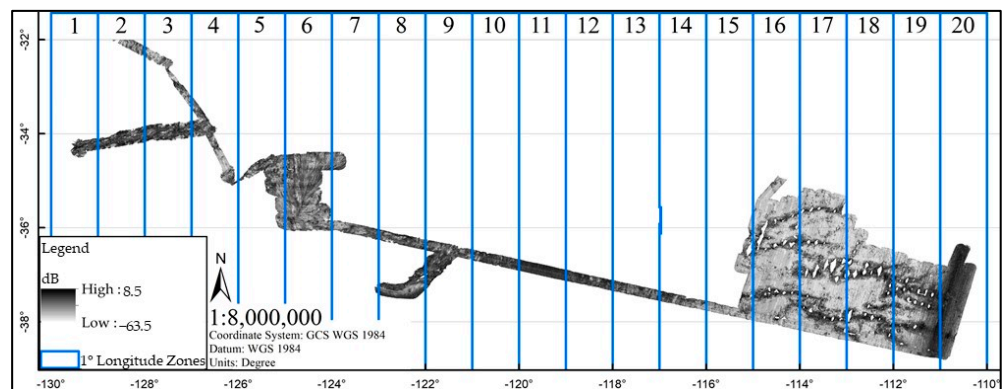


Figure 4. Backscatter data grouped into zones of 1° of longitude, labeled by number at top of figure.

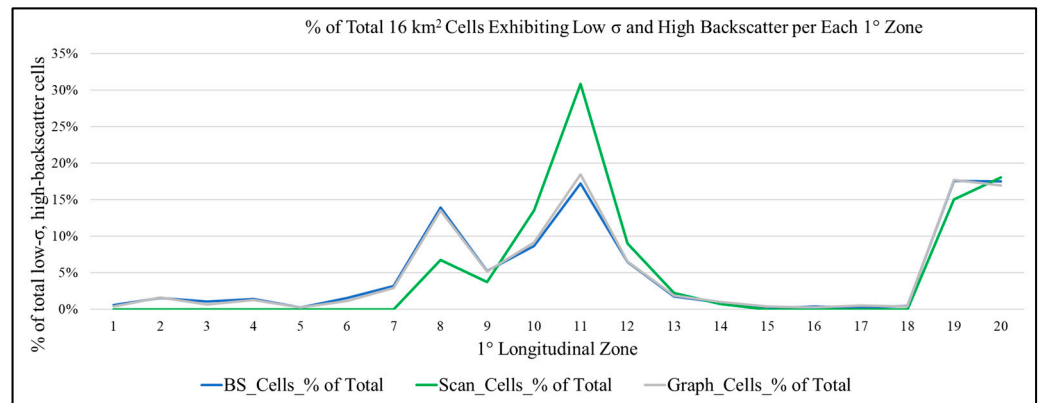


Figure 5. Stack line of all three surfaces showing the percentage of the total high backscatter and low σ cells, from the respective surfaces, present in each 1° longitudinal zone. ‘BS’ (blue line) refers to the backscatter mosaic in dB intensity; ‘Scan’ (green line) refers to the digitized and georeferenced 8-bit graphic paper chart; ‘Graph’ (gray line) refers to the 8-bit backscatter image.

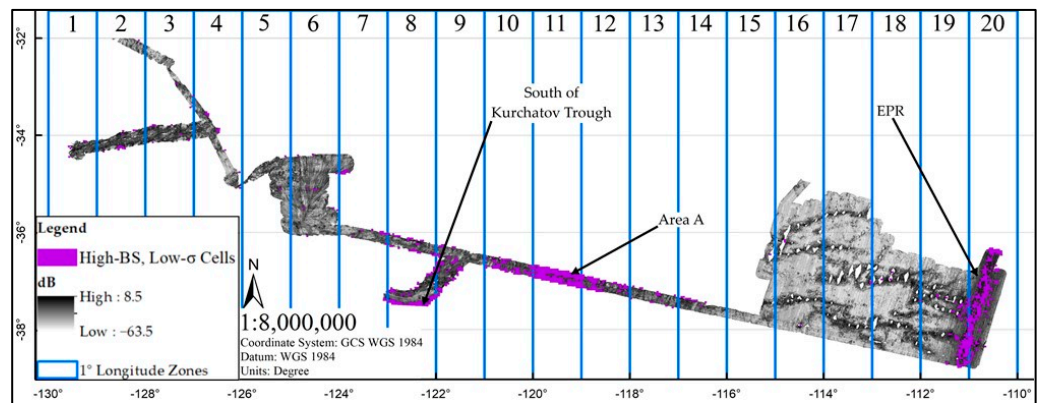


Figure 6. Zonal analysis output for 4 km × 4 km, filtered to areas with low σ and high backscatter values. These zones are shown in purple. Small fractional areas exist within the data, with three apparent clusters labeled in the figure.

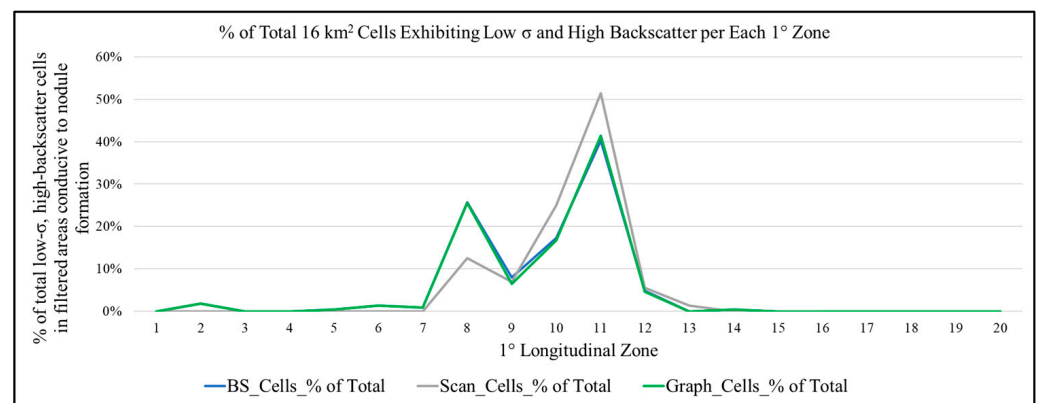


Figure 7. Stack line of all three surfaces, showing the percentage of the total high backscatter and low σ cells, from the respective surfaces, present in each 1° longitudinal zone, as filtered to areas of low slope, water depths below the local CCD, low sedimentation rate, and seafloor > 2 Ma. ‘BS’ (blue line) refers to the backscatter mosaic in dB; ‘Graph’ (green line) refers to the 8-bit backscatter image; ‘Scan’ (gray line) refers to the digitized and georeferenced 8-bit graphic paper chart.

Table 1. Distribution of high-backscatter and low- σ cells by 1° longitudinal zones for each of the three respective surfaces. ‘BS’ refers to the backscatter mosaic in dB; ‘Scan’ refers to the digitized and georeferenced 8-bit graphic paper chart; ‘Graph’ refers to the 8-bit backscatter image.

1° Longitude Zone	BS_Cells_% of Total	Scan_Cells_% of Total	Graph_Cells_% of Total
1	0.59%	0.00%	0.38%
2	1.52%	0.00%	1.63%
3	1.06%	0.00%	0.63%
4	1.41%	0.00%	1.25%
5	0.23%	0.00%	0.25%
6	1.52%	0.00%	1.13%
7	3.17%	0.00%	2.89%
8	13.95%	6.77%	13.55%
9	5.28%	3.76%	5.14%
10	8.68%	13.53%	9.16%
11	17.23%	30.83%	18.44%
12	6.45%	9.02%	6.52%
13	1.76%	2.26%	1.88%
14	0.94%	0.75%	1.00%
15	0.12%	0.00%	0.38%
16	0.35%	0.00%	0.25%
17	0.23%	0.00%	0.50%
18	0.47%	0.00%	0.38%
19	17.58%	15.04%	17.69%
20	17.47%	18.05%	16.94%

Further constraining the high-backscatter, low- σ filtered data to only those geographic areas in the data that are >2 Ma old and accumulating sediment at a rate of 0.3 to <1 cm ka⁻¹, and are also shown by the bathymetry data to be deeper than the local CCD and exhibit a slope $\leq 7^\circ$, identifies the areas most conducive to nodule presence. The three surfaces all identify similar areas within the data, exhibiting homogenous, high backscatter, which, based on bathymetric and geologic context, is attributable to nodule presence. These areas include the Kurchatov trough area (Zone 8) and Area A (Zone 11), with lesser clusters in the adjacent Zones (10 and 12), (Figure 8); the EPR area is excluded based on age and water depth. Similarly to the comparison of the cell distributions prior to filtering by slope, depth, sedimentation rate, and age, the two surfaces created from the digital backscatter data align very closely ($R = 0.999$), and the scanned surface correlates well but not as closely ($R = 0.941$ between ‘backscatter’ and ‘scan’ surfaces, and $R = 0.943$ between ‘graphic’ and ‘scan’ surfaces). For all three surfaces, higher cluster peaks exist in Zones 10, 11, and 12 (Area A and adjacent), with a lower peak in Zone 8 (Kurchatov trough) (Figures 5 and 7; Table 2).

Angular response data from select geographic locations indicated a difference in seafloor substrate among sections of the data. This was determined by both the mean across-track backscatter intensity and the profile shape of the angular response diagram. These locations are shown in Figure 9 and described in Table 3. Figure 10 depicts the angular response of the across-track sites within the data. Figure 11 depicts the same, as well as the modeled, profiles for 15 kHz sonar for a range of substrate types, as described in the handbook [76], and Figure 12 depicts the same, as well as the angular, response at 12 kHz by substrate type, including nodules of ~20 kg/m² and ~40 kg/m² abundance observed at a site in the western Pacific Ocean, adapted from Yang et al. (2020) [46].

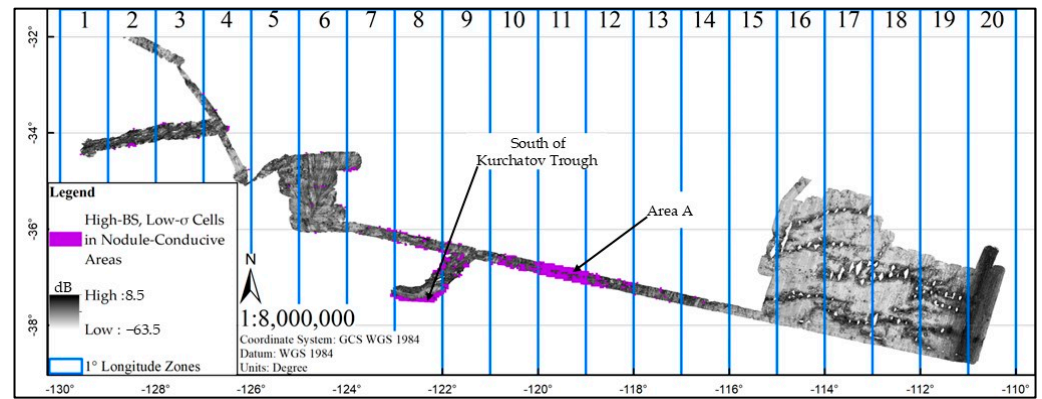


Figure 8. Zonal analysis output for 4 km × 4 km filtered to areas with a low backscatter σ and high backscatter value, and constrained to areas conducive to nodule presence in terms of slope, water depth, sedimentation rate, and seafloor age. Zones likely to contain nodules are shown in purple. Small fractional areas exist within the data, with two apparent clusters labeled in the figure.

Table 2. Distribution of high-backscatter-value and low-backscatter- σ cells by 1° longitudinal zones for each of the three surfaces, constrained to areas conducive to nodule presence in terms of sedimentation rate, water depth, seafloor slope, and seafloor age. Gray-shaded table rows indicate 1° longitudinal zones containing no cells exhibiting both a high backscatter value and low backscatter σ after applying such constraints. ‘Scan’ refers to the digitized and georeferenced 8-bit graphic paper chart; ‘Graph’ refers to the 8-bit backscatter image; ‘BS’ refers to the backscatter mosaic in dB.

1° Longitude Zone	BS_Cells_% of Total	Scan_Cells_% of Total	Graph_Cells_% of Total
1	0.00%	0.00%	0.00%
2	1.77%	0.00%	1.86%
3	0.00%	0.00%	0.00%
4	0.00%	0.00%	0.00%
5	0.44%	0.00%	0.47%
6	1.33%	0.00%	1.40%
7	0.88%	0.00%	0.93%
8	25.66%	12.50%	25.58%
9	7.96%	6.94%	6.51%
10	17.26%	25.00%	16.74%
11	40.27%	51.39%	41.40%
12	4.87%	5.56%	4.65%
13	0.00%	1.39%	0.00%
14	0.44%	0.00%	0.47%
15	0.00%	0.00%	0.00%
16	0.00%	0.00%	0.00%
17	0.00%	0.00%	0.00%
18	0.00%	0.00%	0.00%
19	0.00%	0.00%	0.00%
20	0.00%	0.00%	0.00%

Table 3 shows the sites within the data where cross-track angular response diagrams were generated from the backscatter mosaic, with cell values in dB. The absolute average difference between the diagram trendline and the nadir intercept was used as a marker of the general flatness of the profile, in terms of the range of backscatter values about the trendline intercept. Site 5, corresponding to Area A, exhibits the lowest variability. Site 7, corresponding to the area south of the Kurchatov trough, exhibits the highest variability. Sites 5, 6, 7, and 9 are the only sites with $>1\sigma$ difference across-track between the intercept and the backscatter, indicating these are significantly higher or lower in terms of their profile flatness. Sites 1 and 5 exhibit the highest mean backscatter values. The high mean backscatter and flat profile of Site 5 align with an expected nodule profile, as shown in Figure 12, adapted from Yang et al. (2020) [46].

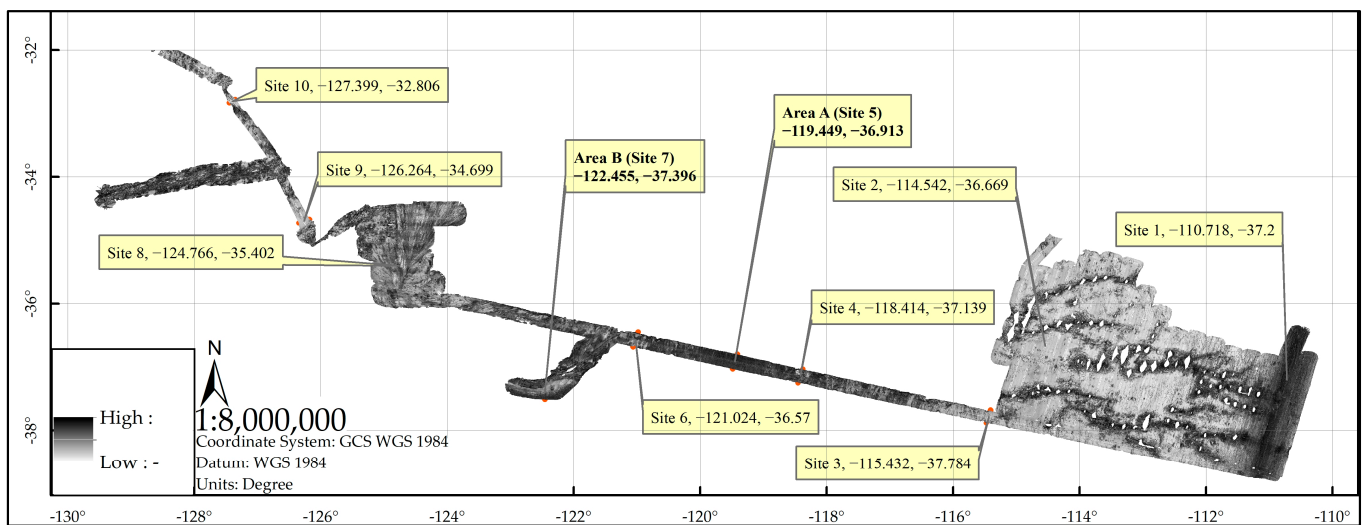


Figure 9. Sites within the backscatter data for which across-track angular response diagrams were generated based on backscatter raster values. Sites are ordered 1 to 10, labeled in the figure and outlined in red, from youngest near EPR to oldest in the furthest northwest extent of the data. Table 3 describes each location.

Table 3. Angular response diagram statistics for 10 test sites from the data. The column ‘Absolute Average Difference between Trendline Intercept and BS at Incidence Angles’ indicates the general flatness of the profile.

Site	Area Name	Mean BS (dB)	Absolute Difference Between Trendline Intercept and Nadir	Absolute Average Difference Between Trendline Intercept and BS at Incidence Angles
1	EPR	−19.69	8.687355	2.29
2	Survey flat area between volcanic features west of EPR	−40.22	11.8692	1.75
3	Transit southeast of/younger than Area A	−36.53	7.593326	2.91
4	Transit slightly southeast of/younger than Area A	−23.49	10.575	2.73
5	Area A	−19.283	1.283	1.10
6	Transit slightly northwest of Area A	−28.5	4.996	4.65
7	Kurchatov trough	−26.14	24.942	5.62
8	Selkirk structure	−27.72	10.829983	3.29
9	Transit north of Selkirk structure, apparent low BS	−39.42	4.057381	1.37
10	Transit in northwest data area, apparent low BS	−42.05	9.019949	2.00

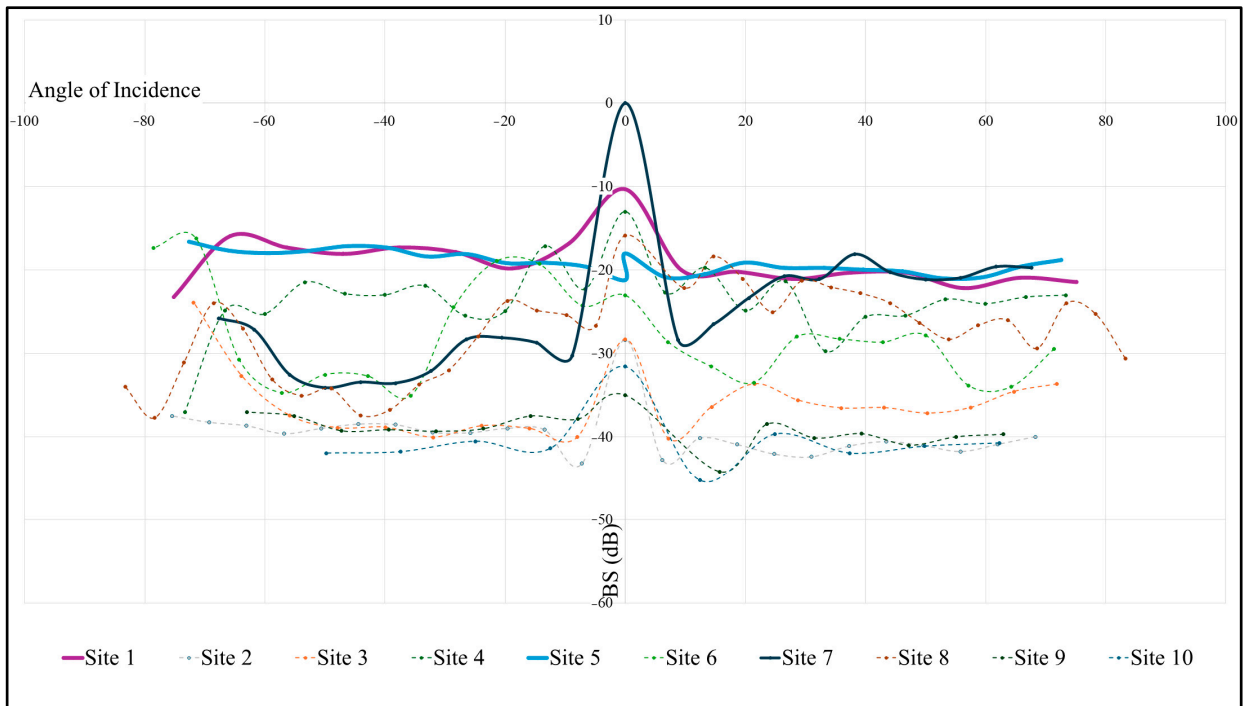


Figure 10. Angular response diagrams from backscatter surface values, in terms of dB. Site descriptions correspond to descriptions in Table 3. Site 5, corresponding to Area A, exhibits the flattest line and highest mean backscatter. Site 1, corresponding to the EPR, exhibits similar backscatter but higher variability. Site 7, corresponding to the Kurchatov trough, shows greater variability, though the 40–60° range aligns with the diagrams of Sites 1 and 5.

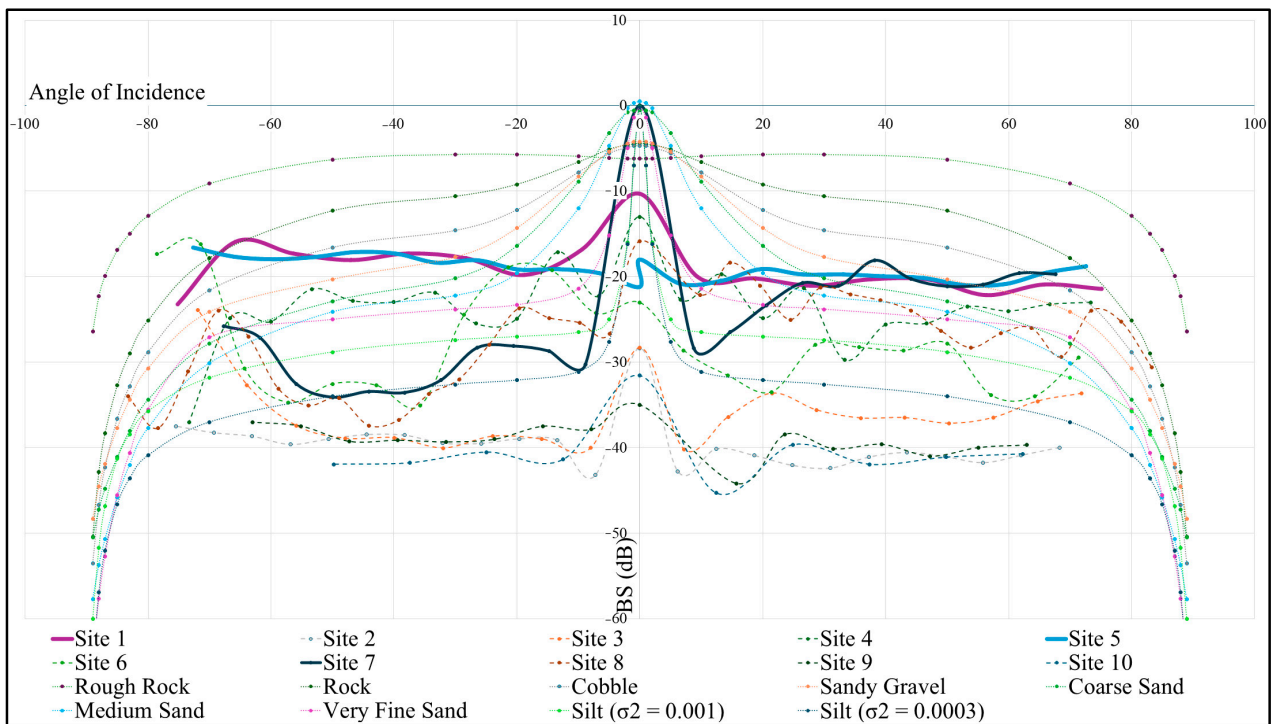


Figure 11. Angular response diagrams from backscatter surface values in terms of dB. Site descriptions correspond to descriptions in Table 3. Model profiles for several substrate types in terms of 15 kHz angular response, as described in the handbook [76], are shown.

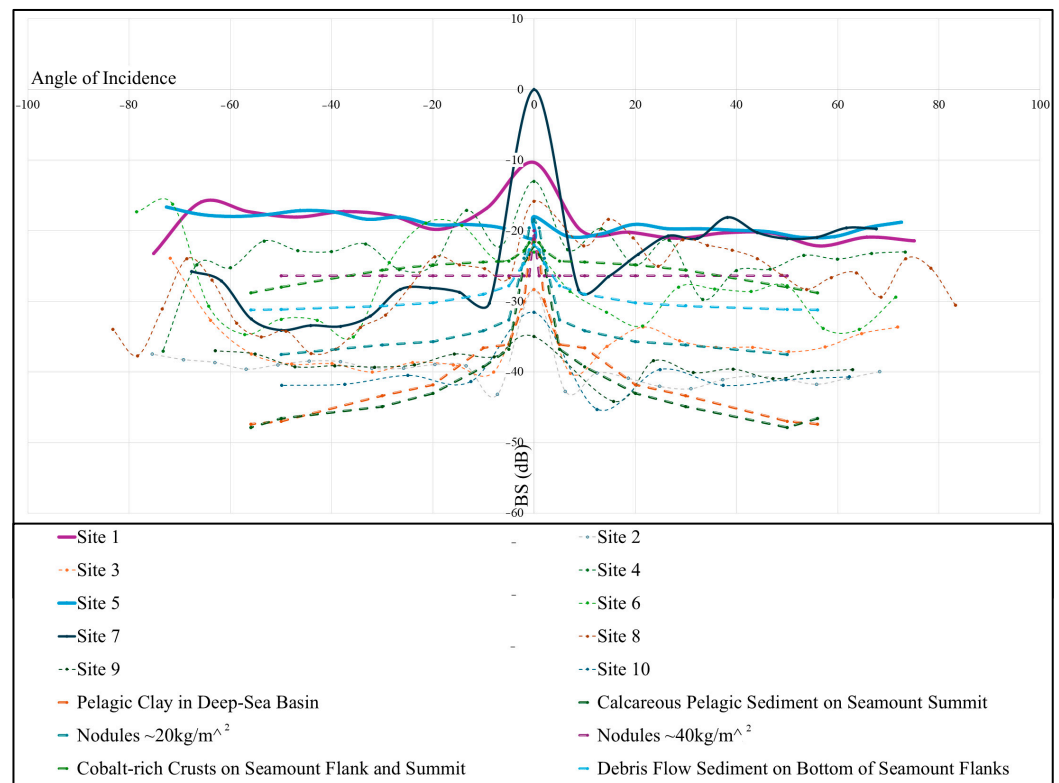


Figure 12. Angular response diagrams from backscatter surface values, in terms of dB. Site descriptions and sediment types correspond to Tables 3 and 4. Model profiles for several substrate types, including nodules at two abundance levels, in terms of 12 kHz angular response from a study site in the western Pacific Ocean, are labeled in the graph (adapted from Yang et al. (2020) [46]). Note relatively high, uniform backscatter values for the 40 kg/m² nodule profile; note relatively high, uniform backscatter values for Site 5 (Area A). This qualitative comparison of angular response diagrams suggests abundant nodules exist in Site 5 (Area A) and partially in Site 7 (southern Kurchatov trough area).

Table 4. Angular response diagram statistics for six seafloor strata types, adapted from Yang et al. (2020) [46]. Column ‘Absolute Average Difference between Trendline Intercept and BS at Incidence Angles’ indicates the general flatness of the profile.

Seafloor Strata Type	Mean BS (dB)	Absolute Difference Between Trendline Intercept and Nadir	Absolute Average Difference Between Trendline Intercept and BS at Incidence Angles
Pelagic Clay in Deep-Sea Basin	−37.16	15.40	7.25
Calcareous Pelagic Sediment on Seamount Summit	−37.34	14.76	8.34
Nodules ~20 kg/m ²	−30.51	12.12	6.29
Nodules ~40 kg/m ²	−25.97	5.97	0.80
Cobalt-rich Crusts on Seamount Flank and Summit	−24.85	3.03	1.83
Debris Flow Sediment on Bottom of Seamount Flanks	−28.03	5.85	2.86

6. Discussion

We performed an analysis of multibeam bathymetry and backscatter data, together with environmental data, to predict nodule occurrences in Area A and the southern Kurchatov trough area. This research considers nodule presence, rather than predicted abundance

in terms of kilograms of nodules per m^2 , because ground-truth data are required to confirm interpretations based solely on multibeam analysis, and would be needed to train an analytical model of nodule abundance based on multibeam backscatter [108]. Although the ability to make quantitative predictions of nodule abundance is beyond the scope of this study, it would certainly be a useful next step for future work, with a focused study that includes ground-truth information.

Across-track angular response diagrams qualitatively reinforce the characterization of nodule presence in Area A (Site 5), while suggesting that a different type of substrate, or a more variable seafloor geology, may exist south of the Kurchatov trough (Site 7). However, the area analyzed for angular response south of the Kurchatov trough only overlaps potential nodule areas with an angle of incidence from $\sim 30^\circ$ to $\sim 70^\circ$ (Figures 10–12). For this section of the Kurchatov trough area (Site 7) angular response diagram, the angular response closely aligns with the respective sections of angular response diagrams of the EPR (Site 1) and Area A (Site 5), indicating that there is nodule presence only in this section of the data area analyzed for Site 7. It must be noted the angular response diagrams were generated from the backscatter raster, and were not taken per-ping.

The extent to which multibeam data editing may have impacted the results is not evident when working only with raster data. Nevertheless, this methodology may provide a more readily attainable means of assessing angular response for scientists without access to digital multibeam data or the specific software needed for generating angular response diagrams. However, this method requires additional effort and inherent imprecision for matching a wide swath from a hull-mounted multibeam system operated in deep water with the most likely average seafloor type in a specific location in the data; if the wide swath encounters an area of apparent variable backscatter, the angular response profile may not match closely with a modeled profile. Without the built-in capability afforded by specialized software, interpretation can prove more challenging for an investigator to accurately, and consistently, determine.

Ideally, calibrated backscatter data can be acquired with a respective system and used as a benchmark. The comparative analysis undertaken in this research relied on profiles described in both the handbook [76], which did not provide a 12 kHz model output, as well as by Yang et al. (2020) [46], which considered data collected in the same ocean and at the same frequency, but with a multibeam system not necessarily intended to be used as a calibrated benchmark to compare with other backscatter data. While backscatter data sets can be adjusted to one another for a direct numerical comparison of backscatter strength or range [109], such normalization when using only uncalibrated data would be arbitrary. As such, the shape of angular response diagrams for respective seafloor types is the comparative factor to consider, irrespective of the system used for collection. This research indicates that the use of angular response diagrams as an evaluative tool works well as a complement to analysis undertaken with bathymetry and backscatter surfaces.

It must be noted, however, that data collected with modern multibeam systems preserve a more accurate backscatter value in terms of across-track intensity variation than older systems, such as the EM12 and EM12D. Data generated by older multibeam systems, such as the case study data used in this research, have more greatly corrected across-track variation before digitization, since these systems lack the dynamic range of modern systems, and require a more complicated, time-varying gain function. Hence, more modern data allow for improved angular response analysis. The agreement between both angular response and backscatter interpretation described in this research may in part have been due to the generation of angular response data from the backscatter surface itself, and the ingrained characteristics of working with an archived data set from the late 20th century.

During this research, similar results were achieved regardless of which of the three backscatter surfaces were used, though the trends were more subdued in the scanned chart. The scanned chart allows for data analysis, but digital products derived by reprocessing the original digital values provide greater data density, which may result in accentuated trends

in pixel distribution graphs. Similarities between the three surfaces may be accentuated owing to processing undertaken during and following the cruise, which may have included treatment in contemporaneous acquisition and processing software suites. Comparing results from additional data sets and products, as well as products produced from additional software suites, may offer future opportunities to address the research question of whether differing backscatter products produced from the same data, but with different software or methods, can provide similar interpretations of seafloor characterization.

This study suggests that backscatter products such as raster surfaces provide a suitable basis for evaluating prospective nodule areas and delineating seafloor substrate types. While assessment relying on raw multibeam data may compliment or refine results based solely on backscatter products, the adaptability of backscatter products in software other than specialized multibeam software may afford more opportunities to a broader range of scientists and persons interested in characterizing seafloor geology.

Explanations for high backscatter intensity other than nodule presence include the presence of abyssal hill outcrops, recent lava flows, or polymetallic crusts. However, the geomorphology of both Area A and the area south of the Kurchatov trough do not indicate the characteristic dendritic patterns of lava flows or sharp contrasts with older sedimented seafloor (e.g., Hagen et al., 1990 [110]). Polymetallic crust presence, e.g., Fe-Mn coating on exposed igneous basement, may be present throughout this general area of the transit, but this coating is not expected to be a predominate feature of Area A, because, unlike nodules, flat crusted seafloor would be buried by sediment in this location. Likewise, the differences in angular responses and the broad areas of high, homogenous backscatter (Figures 10–12) would be best explained by a large nodule field.

Future ground-truth data collection will be needed to test these nodule field predictions and validate the applicability of this method in detecting them. Models based on remote sensing data can be trained with inputs of empirical data to establish nodule domains, as well as geological domains of different seafloor types. Ground-truth data collection will help in developing a future multibeam algorithm to estimate nodule abundance, or delineating nodule deposits by their abundance range within the area included in the case study data.

Differentiating seafloor substrate types will assist with marine spatial planning, as domain types, spatial extents of individual domains, and benthic habitats can be more precisely defined. This may facilitate marine spatial planning initiatives and the fulfillment of objectives such as the protection and conservation designation of 30% of marine area by 2030, as stated in the Kunming-Montreal Global Biodiversity Framework, as well as supporting the ongoing management of marine mineral resources, e.g., the International Seabed Authority [111–114].

All of the data involved in this case study exist in international waters, in an area with seabed resources administered by the United Nations. Area A accounts for ~3000 km² of seafloor, and the potential nodule area south of the Kurchatov trough accounts for ~1000 km² of seafloor. The estimated area of seafloor that is prospective for abundant nodules in the Pacific Ocean is ~28,000,000 km² from nine areas, ranging from ~350,000 km² to ~8,000,000 km² [34]. Should Area A and the surrounding region be confirmed to contain abundant nodule fields, this would contribute to estimates of the Pacific seafloor containing nodules, and would support efforts to classify benthic habitat domains throughout the Pacific. Similar high-resolution data are scarce in the region; low-resolution bathymetric estimates, and the application of filters for environmental parameters conducive to nodule presence, suggest that the occurrences indicated in this case study's data may be part of a much larger occurrence. As more of the world's oceans are mapped in high resolution, new data may show this area as a continuance of known occurrences in the southern Pacific Ocean, or as a unique contiguous field, unconnected to known occurrences. Future multibeam data collection, particularly adjacent to the data boundary to the south and east of the Kurchatov trough area, as well as north and south of Area A, would enable such an assessment.

7. Conclusions

Analysis indicates that Area A and the area south of the Kurchatov trough contain polymetallic nodule occurrences. This is based on their respective data being characterized by homogenous, high backscatter values, and the application of bathymetric and geologic context. Zonal analysis of the data indicates a higher concentration of 16 km² cells exhibiting high backscatter values and low heterogeneity within Area A than elsewhere in the data. This is true whether or not the data are constrained to areas conducive to nodule formation. The zone including the Kurchatov trough exhibits the second-highest concentration of such cells when constraining to areas conducive to nodule formation, while the EPR exhibits the second-highest concentration of such cells when the constraints for nodule formation are not met, and where known recent volcanism exists [83]. The scanned paper chart contains a higher proportion of such cells in Area A than do the reprocessed digital backscatter products; likewise, clusters of such cells are less apparent in the scanned paper chart results mapping these data, perhaps owing to the higher resolution of the digital backscatter mosaics and grayscale images.

A relative seafloor valley slightly below the CCD exists in and immediately adjacent to Area A, while low-slope seafloor of ~4500 m water depth exists to the south of the Kurchatov trough. The results suggest that smaller areas within the data may also contain nodules, though their proximity to tectonic structures limits their expanse compared to Area A and the plain south of the Kurchatov trough. Qualitative assessments of angular response diagrams generated from select locations throughout the data indicate differing geological characteristics, and reinforce the interpretation of nodule presence where it is suggested by bathymetry, backscatter value, and environmental parameters. Although ground-truth sample data are required to validate the characteristics of seafloor geological domains, this research strongly suggests that transit multibeam bathymetry and backscatter data, including angular response, can be used in combination with geologic and environmental data, prior to ground-truth data collection, to predict areas of deep seafloor that are likely to contain polymetallic nodules.

The primary variables for identifying areas likely to contain polymetallic nodules are homogeneous, strong multibeam backscatter data in areas of seafloor older than 2 Ma that are deeper than the CCD, subject to sedimentation rates of 3 to <10 mm ka⁻¹, and have an overall seafloor slope $\leq 7^\circ$. Based on this proposed method, we predict that the evidence from a single multibeam transit indicates two areas of ~3000 km² and ~1000 km², in water depths > 4000 m, that contain nodule occurrences. These locations are limited to the extent of the data. Future use of similar methods may be used with low-resolution bathymetric estimates of adjacent areas to identify whether a much more expansive occurrence may exist in the region, though angular response analysis would not be possible, and the results would only be indirectly comparable, owing to poorer bathymetric resolution. Future work may also include a data mining exercise to locate geological samples coincident with the data collected, using the same multibeam system in comparable water depths; this would allow for an additional case study, and provide an empirical basis for interpreting the angular response diagrams generated in this study.

Lastly, considering the vast amount of archived multibeam transit data from remote areas of the world's oceans, and the new multibeam data expected from the Seabed 2030 Project [115–119], we propose that this type of first-order analysis could be useful as a cost-effective, desk-based analytical method for determining other potential nodule fields, using a specific set of variables, including multibeam backscatter data exhibiting high values and homogeneity (along- and across-track), geomorphology from multibeam bathymetry, environmental parameters conducive to nodule formation, and angular response profiles fitting a shape and intensity that represents a high-impedance, high-rugosity seafloor. This proposed method could help to prioritize future exploration activities, including transit planning to or from focused survey areas, and could assist scientists and regulators in estimating marine ecological and mineral resources. Additional industrial applications for characterizing seafloor geology with these methods include cable route

surveys, locating seamounts or other features which could pose a navigation hazard, and identifying types of seafloor habitats.

Supplementary Materials: The following supporting information can be downloaded at: <https://www.mdpi.com/article/10.3390/jmse12122322/s1>.

Author Contributions: Conceptualization, D.F.N.; Methodology, M.M. and M.K.; Software, D.W.C.; Data curation, and M.M.; Writing—original draft, M.E.M.; Writing—review & editing, T.A.C. and A.G.C.G. All authors have read and agreed to the published version of the manuscript.

Funding: This research was enhanced through a cooperative agreement between NOAA's Office of Coast Survey and the University of South Florida through the Center for Ocean Mapping and Innovative Technologies (COMIT), NA20NOS4000227. The Foundation-Hotline cruise ship time was funded by grants to the Flotte Océanographique Française and was supported by INSU-CNRS, with research funded by INSU-CNRS program Interieur de la Terre, grant 97N51/0349.

Institutional Review Board Statement: Not applicable.

Informed Consent Statement: Not applicable.

Data Availability Statement: Data are contained within the article and Supplementary Materials.

Acknowledgments: This work has benefited from funding and discussions within the NOAA-USF Center for Ocean Mapping and Innovative Technologies (COMIT). Additional details related to this work can be found within the online thesis (Mussett, 2023) [68].

Conflicts of Interest: Author Mark Mussett was employed by the company Odyssey Marine Exploration, and authors Max Kaufmann and Tracey A. Conrad were contracted by the same company. This company provided no funding for this research. These authors' work on this paper presents no conflict of interest. Anyone including other companies and academic institutions are free to test these predictions with no conflict. The remaining authors declare that the research was conducted. absence of any commercial or financial relationships that could be construed as a potential conflict of interest.

References

1. Hein, J.R.; Koschinsky, A. Deep-Ocean Ferromanganese Crusts and Nodules. In *Treatise on Geochemistry*; Elsevier: Amsterdam, The Netherlands, 2014; Volume 13, pp. 273–291.
2. Kodagali, V.N.; Chakraborty, B. Multibeam Echosounder Pseudo Sidescan Images as a Tool for Manganese Nodule Exploration. In Proceedings of the ISOPE Ocean Mining and Gas Hydrates Symposium, Goa, India, 8–10 November 1999; pp. 97–104.
3. Kuhn, T.; Wegorzewski, A.; Rühlemann, C.; Vink, A. Composition, Formation, and Occurrence of Polymetallic Nodules. In *Deep-Sea Mining: Resource Potential, Technical and Environmental Considerations*; Sharma, R., Ed.; Springer International Publishing: Cham, Switzerland, 2017; pp. 23–63, ISBN 978-3-319-52557-0.
4. Mero, J.L. *The Mineral Resources of the Sea*; Elsevier: Amsterdam, The Netherlands, 1965; Volume 1.
5. Verlaan, P.A.; Cronan, D.S. Origin and Variability of Resource-Grade Marine Ferromanganese Nodules and Crusts in the Pacific Ocean: A Review of Biogeochemical and Physical Controls. *Geochemistry* **2022**, *82*, 125741. [CrossRef]
6. Tao, C.; Jin, X.; Bian, A.; Li, H.; Deng, X.; Zhou, J.; Gu, C.; Wu, T.; Roy, W. Estimation of Manganese Nodule Coverage Using Multi-Beam Amplitude Data. *Mar. Georesour. Geotechnol.* **2015**, *33*, 288–293. [CrossRef]
7. Glasby, G.P. *Marine Manganese Deposits*; Elsevier Oceanography Series, 15; Glasby, G.P., Ed.; Elsevier North-Holland Inc.: Amsterdam, The Netherlands, 1977; Volume 15.
8. Cronan, D.S. Deep Sea Minerals. *Geoscientist* **2015**, *25*, 10–15.
9. Kuhn, T.; Uhlenkott, K.; Vink, A.; Rühlemann, C.; Martinez Arbizu, P. Chapter 58—Manganese Nodule Fields from the Northeast Pacific as Benthic Habitats. In *Seafloor Geomorphology as Benthic Habitat*, 2nd ed.; Harris, P.T., Baker, E., Eds.; Elsevier: Amsterdam, The Netherlands, 2020; pp. 933–947, ISBN 978-0-12-814960-7.
10. Abramowski, T.; Stoyanova, V. Deep-Sea Polymetallic Nodules: Renewed Interest as Resources for Environmentally Sustainable Development. In Proceedings of the 12th International Multidisciplinary Scientific GeoConference SGEM 2012, Albena, Bulgaria, 17–23 June 2012; pp. 515–521.
11. Alevizos, E.; Schoening, T.; Koeser, K.; Snellen, M.; Greinert, J. Quantification of the Fine-Scale Distribution of Mn Nodules: Insights from AUV Multi-Beam and Optical Imagery Data Fusion. *Biogeosci. Discuss.* **2018**, preprint. [CrossRef]
12. Alvarenga, R.A.F.; Pr at, N.; Duhayon, C.; Dewulf, J. Prospective Life Cycle Assessment of Metal Commodities Obtained from Deep-Sea Polymetallic Nodules. *J. Clean. Prod.* **2022**, *330*, 129884. [CrossRef]
13. Glasby, G.P.; Li, J.; Sun, Z. Deep-Sea Nodules and Co-Rich Mn Crusts. *Mar. Georesour. Geotechnol.* **2015**, *33*, 72–78. [CrossRef]
14. Hein, J.R.; Spinardi, F.; Tawake, A.; Mizell, K.; Thorburn, D. Critical metals in manganese nodules from the Cook Islands EEZ. In Proceedings of the 42nd Underwater Mining Institute, Rio de Janeiro, Brazil, 21–29 October 2013.

15. Hein, J.R.; Spinardi, F.; Okamoto, N.; Mizell, K.; Thorburn, D.; Tawake, A. Critical Metals in Manganese Nodules from the Cook Islands EEZ, Abundances and Distributions. *Ore Geol. Rev.* **2015**, *68*, 97–116. [[CrossRef](#)]
16. Hein, J.R.; Koschinsky, A.; Kuhn, T. Deep-Ocean Polymetallic Nodules as a Resource for Critical Materials. *Nat. Rev. Earth Environ.* **2020**, *1*, 158–169. [[CrossRef](#)]
17. Kuhn, T.; Rühlemann, C. Exploration of Polymetallic Nodules and Resource Assessment: A Case Study from the German Contract Area in the Clarion-Clipperton Zone of the Tropical Northeast Pacific. *Minerals* **2021**, *11*, 618. [[CrossRef](#)]
18. Ma, Y.; Magnuson, A.H.; Varadan, V.K.; Varadan, V.V. Acoustic Response of Manganese Nodule Deposits. *Geophysics* **1986**, *51*, 689–698. [[CrossRef](#)]
19. Petersen, S.; Krättschell, A.; Augustin, N.; Jamieson, J.; Hein, J.R.; Hannington, M.D. News from the Seabed—Geological Characteristics and Resource Potential of Deep-Sea Mineral Resources. *Mar. Policy* **2016**, *70*, 175–187. [[CrossRef](#)]
20. Purser, A.; Marcon, Y.; Hoving, H.-J.T.; Vecchione, M.; Piatkowski, U.; Eason, D.; Bluhm, H.; Boetius, A. Association of Deep-Sea Incirrate Octopods with Manganese Crusts and Nodule Fields in the Pacific Ocean. *Curr. Biol.* **2016**, *26*, R1268–R1269. [[CrossRef](#)]
21. Rühlemann, C.; Kuhn, T.; Wiedicke, M.; Kasten, S.; Mewes, K.; Picard, A. Current Status of Manganese Nodule Exploration in the German License Area. In Proceedings of the ISOPE Ocean Mining and Gas Hydrates Symposium, Maui, HI, USA, 19–24 June 2011; ISBN 978-1-880653-95-1.
22. Vanreusel, A.; Hilario, A.; Ribeiro, P.A.; Menot, L.; Arbizu, P.M. Threatened by Mining, Polymetallic Nodules Are Required to Preserve Abyssal Epifauna. *Sci. Rep.* **2016**, *6*, 26808. [[CrossRef](#)] [[PubMed](#)]
23. Wang, X.; Müller, W.E.G. Marine Biominerals: Perspectives and Challenges for Polymetallic Nodules and Crusts. *Trends Biotechnol.* **2009**, *27*, 375–383. [[CrossRef](#)] [[PubMed](#)]
24. Hein, J.R.; Mizell, K. Chapter 8 Deep-Ocean Polymetallic Nodules and Cobalt-Rich Ferromanganese Crusts in the Global Ocean: New Sources for Critical Metals. In *The United Nations Convention on the Law of the Sea, Part XI Regime and the International Seabed Authority: A Twenty-Five Year Journey*; Brill | Nijhoff: Leiden, The Netherlands, 2022; pp. 177–197, ISBN 978-90-04-50738-8.
25. Baturin, G.N. Mineral Resources of the Sea. *Lithol. Miner. Resour.* **2000**, *35*, 399–424. [[CrossRef](#)]
26. Dutkiewicz, A.; Judge, A.; Müller, R.D. Environmental Predictors of Deep-Sea Polymetallic Nodule Occurrence in the Global Ocean. *Geology* **2020**, *48*, 293–297. [[CrossRef](#)]
27. Exon, N.F.; Cronan, D.S.; Colwell, J.B. New Developments in Manganese Nodule Prospects, with Emphasis on the Australasian Region. In Proceedings of the Pacific Rim Congress 90. An International Congress on the Geology, Structure, Mineralisation, Economics and Feasibility of Mining Developments in the Pacific Rim. Including Feasibility Studies of Mines in Remote, Island, Rugged and High Rainfall Locations, Gold Coast, Australia, 6 May 1990; pp. 363–371.
28. Glasby, G.P.; Stoffers, P.; Sioulas, A.; Thijssen, T.; Friedrich, G. Manganese Nodule Formation in the Pacific Ocean: A General Theory. *Geo-Mar. Lett.* **1982**, *2*, 47–53. [[CrossRef](#)]
29. Ko, Y.; Lee, S.; Kim, J.; Kim, K.-H.; Jung, M.-S. Relationship between Mn Nodule Abundance and Other Geological Factors in the Northeastern Pacific: Application of GIS and Probability Method. *Ocean. Sci. J.* **2006**, *41*, 149–161. [[CrossRef](#)]
30. Lusty, P.A.J.; Murton, B.J. Deep-Ocean Mineral Deposits: Metal Resources and Windows into Earth Processes. *Elements* **2018**, *14*, 301–306. [[CrossRef](#)]
31. Mckelvey, V.E. *Subsea Mineral Resources*; USGS: Reston, VA, USA, 1986.
32. Mckelvey, V.E.; Wright, N.A.; Bowen, R.W. *Analysis of the World Distribution of Metal-Rich Subsea Manganese Nodules*; USGS: Reston, VA, USA, 1983.
33. McKelvey, V.E.; Wang, F.F.H. *World Subsea Mineral Resources*; United States Geological Survey: Reston, VA, USA, 1969; p. 17.
34. Mizell, K.; Hein, J.R.; Au, M.; Gartman, A. Estimates of Metals Contained in Abyssal Manganese Nodules and Ferromanganese Crusts in the Global Ocean Based on Regional Variations and Genetic Types of Nodules. In *Perspectives on Deep-Sea Mining: Sustainability, Technology, Environmental Policy and Management*; Sharma, R., Ed.; Springer International Publishing: Cham, Switzerland, 2022; pp. 53–80, ISBN 978-3-030-87982-2.
35. Murton, B.J. A Global Review of Non-Living Resources on the Extended Continental Shelf. *Rev. Bras. Geofísica* **2000**, *18*, 281–306. [[CrossRef](#)]
36. Rona, P.A. Resources of the Sea Floor. *Science* **2003**, *299*, 673–674. [[CrossRef](#)]
37. Rona, P.A. The Changing Vision of Marine Minerals. *Ore Geol. Rev.* **2008**, *33*, 618–666. [[CrossRef](#)]
38. Kaufmann, M. *The Hunt for Deep-Sea Minerals—Identifying and Analysing Formation Areas of Marine Minerals*; University of Exeter: Exeter, UK, 2020; [Unpublished].
39. Cronan, D.S. *Underwater Minerals*; Academic Press: Cambridge, MA, USA, 1980.
40. Moustier, C. Inference of Manganese Nodule Coverage from Sea Beam Acoustic Backscattering Data. *Geophysics* **1985**, *50*, 989–1001. [[CrossRef](#)]
41. Machida, S.; Sato, T.; Yasukawa, K.; Nakamura, K.; Iijima, K.; Nozaki, T.; Kato, Y. Visualisation Method for the Broad Distribution of Seafloor Ferromanganese Deposits. *Mar. Georesour. Geotechnol.* **2021**, *39*, 267–279. [[CrossRef](#)]
42. Masson, D.G.; Scanlon, K.M. Comment on the Mapping of Iron-Manganese Nodule Fields Using Reconnaissance Sonars Such as GLORIA. *Geo-Mar. Lett.* **1993**, *13*, 244–247. [[CrossRef](#)]
43. Scanlon, K.M.; Masson, D.G. Fe-Mn Nodule Field Indicated by GLORIA, North of the Puerto Rico Trench. *Geo-Mar. Lett.* **1992**, *12*, 208–213. [[CrossRef](#)]

44. Weydert, M.M.P. Measurements of the Acoustic Backscatter of Selected Areas of the Deep Seafloor and Some Implications for the Assessment of Manganese Nodule Resources. *J. Acoust. Soc. Am.* **1990**, *88*, 350–366. [[CrossRef](#)]
45. Weydert, M.M.P. Measurements of the Acoustic Backscatter of Manganese Nodules. *J. Acoust. Soc. Am.* **1985**, *78*, 2115–2121. [[CrossRef](#)]
46. Yang, Y.; He, G.; Ma, J.; Yu, Z.; Yao, H.; Deng, X.; Liu, F.; Wei, Z. Acoustic Quantitative Analysis of Ferromanganese Nodules and Cobalt-Rich Crusts Distribution Areas Using EM122 Multibeam Backscatter Data from Deep-Sea Basin to Seamount in Western Pacific Ocean. *Deep.-Sea Res. Part I Oceanogr. Res. Pap.* **2020**, *161*, 103281. [[CrossRef](#)]
47. Brown, C.J.; Beaudoin, J.; Brissette, M.; Gazzola, V. Multispectral Multibeam Echo Sounder Backscatter as a Tool for Improved Seafloor Characterization. *Geosciences* **2019**, *9*, 126. [[CrossRef](#)]
48. Alevizos, E.; Huvenne, V.A.I.; Schoening, T.; Simon-Lledó, E.; Robert, K.; Jones, D.O.B. Linkages between Sediment Thickness, Geomorphology and Mn Nodule Occurrence: New Evidence from AUV Geophysical Mapping in the Clarion-Clipperton Zone. *Deep.-Sea Res. Part I Oceanogr. Res. Pap.* **2022**, *179*, 103645. [[CrossRef](#)]
49. Chakraborty, B.; Pathak, D.; Sudhakar, M.; Raju, Y.S. Determination of Nodule Coverage Parameters Using Multibeam Normal Incidence Echo Characteristics: A Study in the Indian Ocean. *Mar. Georesour. Geotechnol.* **1997**, *15*, 33–48. [[CrossRef](#)]
50. Chakraborty, B.; Kodagali, V. Characterizing Indian Ocean Manganese Nodule-Bearing Seafloor Using Multi-Beam Angular Backscatter. *Geo-Mar. Lett.* **2004**, *24*, 8–13. [[CrossRef](#)]
51. Cui, X.; Liu, H.; Fan, M.; Ai, B.; Ma, D.; Yang, F. Seafloor Habitat Mapping Using Multibeam Bathymetric and Backscatter Intensity Multi-Features SVM Classification Framework. *Appl. Acoust.* **2021**, *174*, 107728. [[CrossRef](#)]
52. Dewolfe, J.; Ling, P. NI 43-101 Technical Report for the NORI Clarion-Clipperton Zone Project, Pacific Ocean. 2018. Available online: <https://www.sedarplus.ca/csa-party/records/document.html?id=64f193433b978c3f48d0856215ad467881abafc5bcb672a774c2c0a0cc4b2067.pdf> (accessed on 4 September 2021).
53. Flentje, W.; Lee, S.E.; Virnovskaia, A.; Wang, S.; Zabeen, S.; Sheno, R.; Wilson, P.; Bennett, S. Polymetallic Nodule Mining: Innovative Concepts for Commercialisation. 2012. Available online: https://www.southampton.ac.uk/assets/imported/transforms/content-block/UsefulDownloads_Download/CDE4EFF4E0D2433993F8C65F3759BF25/LRET%20Collegium%202012%20Volume%205.pdf (accessed on 4 January 2019).
54. Gazis, I.Z.; Schoening, T.; Alevizos, E.; Greinert, J. Quantitative Mapping and Predictive Modeling of Mn Nodules' Distribution from Hydroacoustic and Optical AUV Data Linked by Random Forests Machine Learning. *Biogeosciences* **2018**, *15*, 7347–7377. [[CrossRef](#)]
55. Huggett, Q.J.; Somers, M.L. Possibilities of Using the GLORIA System for Manganese Nodule Assessment. *Mar. Geophys. Res.* **1988**, *9*, 255–264. [[CrossRef](#)]
56. Lee, S.H.; Kim, K.H. Side-Scan Sonar Characteristics and Manganese Nodule Abundance in the Clarion-Clipperton Fracture Zones, NE Equatorial Pacific. *Mar. Georesour. Geotechnol.* **2004**, *22*, 103–114. [[CrossRef](#)]
57. Lipton, I.T.; Nimmo, J.M.; Parianos, J.M. *Technical Report TOML Clarion Clipperton Zone Project, Pacific Ocean*; AMC Consultants Pty Ltd.: Melbourne, VIC, Australia, 2016.
58. Lipton, I.T.; Nimmo, J.M.; Stevenson, I. *Technical Report NORI Area D Clarion Clipperton Zone Mineral Resource Estimate*; AMC Consultants Pty Ltd.: Melbourne, VIC, Australia, 2019.
59. Lipton, I.T.; Nimmo, J.M.; Stevenson, I. *Technical Report NORI Area D Clarion Clipperton Zone Mineral Resource Estimate*; AMC Consultants Pty Ltd.: Melbourne, VIC, Australia, 2021.
60. Machida, S.; Fujinaga, K.; Ishii, T.; Nakamura, K.; Hirano, N.; Kato, Y. Geology and Geochemistry of Ferromanganese Nodules in the Japanese Exclusive Economic Zone around Minamitorishima Island. *Geochem. J.* **2016**, *50*, 539–555. [[CrossRef](#)]
61. Matsushima, J.; Kobayashi, H.; Tanaka, S. Acoustic Backscattering Properties of Manganese Nodules: Numerical and Laboratory Experiments Based on Sub-Bottom Acoustic Profile Surveys. *Mar. Georesour. Geotechnol.* **2022**, *41*, 969–990. [[CrossRef](#)]
62. Meyer, L.; Halkyard, J.; Boda, M.; Felix, D. Nodule Abundance Estimation-The Search for “Good Enough”. In Proceedings of the 42nd Underwater Mining Institute, Rio de Janeiro, Brazil, 21–29 October 2013.
63. Parianos, J.; Lipton, I.; Nimmo, M. Aspects of Estimation and Reporting of Mineral Resources of Seabed Polymetallic Nodules: A Contemporaneous Case Study. *Minerals* **2021**, *11*, 200. [[CrossRef](#)]
64. Peukert, A.; Schoening, T.; Alevizos, E.; Köser, K.; Kwasnitschka, T.; Greinert, J. Understanding Mn-Nodule Distribution and Evaluation of Related Deep-Sea Mining Impacts Using AUV-Based Hydroacoustic and Optical Data. *Biogeosciences* **2018**, *15*, 2525–2549. [[CrossRef](#)]
65. Pillai, R.; Varghese, S.; Prasad, P.D. A Multi-Proxy Approach for Delineation of Ferromanganese Mineralization from the West Sewell Ridge, Andaman Sea. *Mar. Georesour. Geotechnol.* **2023**, *41*, 1440–1464. [[CrossRef](#)]
66. Wang, M.; Wu, Z.; Best, J.; Yang, F.; Li, X.; Zhao, D.; Zhou, J. Using Multibeam Backscatter Strength to Analyze the Distribution of Manganese Nodules: A Case Study of Seamounts in the Western Pacific Ocean. *Appl. Acoust.* **2021**, *173*, 107729. [[CrossRef](#)]
67. Yoo, C.M.; Joo, J.; Lee, S.H.; Ko, Y.; Chi, S.-B.; Kim, H.J.; Seo, I.; Hyeong, K. Resource Assessment of Polymetallic Nodules Using Acoustic Backscatter Intensity Data from the Korean Exploration Area, Northeastern Equatorial Pacific. *Ocean. Sci. J.* **2018**, *53*, 381–394. [[CrossRef](#)]
68. Mussett, M. Mining Multibeam Transit Data for Deep Ocean Polymetallic Nodules: Case Study in Southeast Pacific Ocean. Master's Thesis, University of South Florida, Tampa, FL, USA, 2023.

69. Augustin, J.M.; Suave, R.L.; Lurton, X.; Voisset, M.; Dugelay, S.; Satra, C. Contribution of the Multibeam Acoustic Imagery to the Exploration of the Sea-Bottom. *Mar. Geophys. Res.* **1996**, *18*, 459–486. [CrossRef]
70. Lamarche, G.; Lurton, X.; Anne-Laure, J.-M.V. Augustin 2011_Lamarche_quantitative Characterisation of Seafloor Substrate and Bedforms. *Cont. Shelf Res.* **2011**, *31*, S93–S109. [CrossRef]
71. Lucieer, V.; Roche, M.; Degrendele, K.; Malik, M.; Dolan, M.; Lamarche, G. User Expectations for Multibeam Echo Sounders Backscatter Strength Data-Looking Back into the Future. *Mar. Geophys. Res.* **2018**, *39*, 23–40. [CrossRef]
72. Lurton, X.; Lamarche, G.; Brown, C.; Lucieer, V.; Rice, G.; Schimel, A.; Weber, T.; Backscatter Measurements by Seafloor-Mapping Sonars. Guidelines and Recommendations A Collective Report by Members of the GeoHab Backscatter Working Group. 2015. Available online: https://webstatic.niwa.co.nz/static/BWSG_REPORT_MAY2015_web.pdf (accessed on 6 April 2023).
73. Schimel, A.C.G.; Beaudoin, J.; Parnum, I.M.; Bas, T.L.; Schmidt, V.; Keith, G.; Ierodiaconou, D. Multibeam Sonar Backscatter Data Processing. *Mar. Geophys. Res.* **2018**, *39*, 121–137. [CrossRef]
74. Huang, Z.; Siwabessy, J.; Nichol, S.; Anderson, T.; Brooke, B. Predictive Mapping of Seabed Cover Types Using Angular Response Curves of Multibeam Backscatter Data: Testing Different Feature Analysis Approaches. *Cont. Shelf Res.* **2013**, *61–62*, 12–22. [CrossRef]
75. Fonseca, L.; Brown, C.; Calder, B.; Mayer, L.; Rzhonov, Y. Angular Range Analysis of Acoustic Themes from Stanton Banks Ireland: A Link between Visual Interpretation and Multibeam Echosounder Angular Signatures. *Appl. Acoust.* **2009**, *70*, 1298–1304. [CrossRef]
76. Applied Physics Laboratory, University of Washington. *APL-UW High-Frequency Ocean Environmental Acoustic Models Handbook*; Defense Technical Information Center: Fort Belvoir, VA, USA, 1994; p. 210.
77. Misiuk, B.; Brown, C.J. Multiple Imputation of Multibeam Angular Response Data for High Resolution Full Coverage Seabed Mapping. *Mar. Geophys. Res.* **2022**, *43*, 7. [CrossRef]
78. Haris, K.; Chakraborty, B.; Ingole, B.; Menezes, A.; Srivastava, R. Seabed Habitat Mapping Employing Single and Multi-Beam Backscatter Data: A Case Study from the Western Continental Shelf of India. *Cont. Shelf Res.* **2012**, *48*, 40–49. [CrossRef]
79. Che Hasan, R.; Ierodiaconou, D.; Laurenson, L.; Schimel, A. Integrating Multibeam Backscatter Angular Response, Mosaic and Bathymetry Data for Benthic Habitat Mapping. *PLoS ONE* **2014**, *9*, e97339. [CrossRef]
80. Clarke, J.H. Toward Remote Seafloor Classification Using the Angular Response of Acoustic Backscattering: A Case Study from Multiple Overlapping GLORIA Data. *IEEE J. Ocean. Eng.* **1994**, *19*, 112–127. [CrossRef]
81. Clarke, J.H.; Danforth, B.W.; Valentine, P. Areal Seabed Classification Using Backscatter Angular Response at 95 kHz. In Proceedings of the NATO SAACLANTCEN Conference Proceedings Series CP-45, High Frequency Acoustics in Shallow Water, Lerici, Italy, 30 June–4 July 1997.
82. Maia, M.; FOUNDATION-HOTLINE Cruise. RV L'Atalante. 1997. Available online: <https://campagnes.flotteoceanographique.fr/campagnes/97010010/> (accessed on 1 October 2019).
83. Maia, M.; Ackermann, D.; Dehghani, G.A.; Gente, P.; Hékinian, R.; Naar, D.; O'connor, J.; Perrot, K.; Morgan, J.P.; Ramillien, G.; et al. The Pacific-Antarctic Ridge-Foundation Hotspot Interaction: A Case Study of a Ridge Approaching a Hotspot. *Mar. Geol.* **2000**, *167*, 61–84. [CrossRef]
84. Google Earth™/KML Files | U.S. Geological Survey. Available online: <https://www.usgs.gov/programs/earthquake-hazards/google-earthtkml-files> (accessed on 26 October 2023).
85. Müller, D.; Zahirovic, S.; Williams, S.; Cannon, J.; Seton, M.; Bower, D.; Tetley, M.; Heine, C.; Breton, E.L.; Liu, S.; et al. A Global Plate Model Including Lithospheric Deformation Along Major Rifts and Orogens Since the Triassic. *Tectonics* **2019**, *38*, 1884–1907. [CrossRef]
86. Blais, A.; Gente, P.; Maia, M.; Naar, D.F. A History of the Selkirk Paleomicroplate. *Tectonophysics* **2002**, *359*, 157–169. [CrossRef]
87. Mizell, K.; Hein, J.R. Ocean Floor Manganese Deposits. In *Encyclopedia of Geology*, 2nd ed.; Alderton, D., Elias, S.A., Eds.; Academic Press: Oxford, UK, 2021; pp. 993–1001, ISBN 978-0-08-102909-1.
88. Glasby, G.P. Manganese: Predominant Role of Nodules and Crusts. In *Marine Geochemistry*; Schulz, H.D., Zabel, M., Eds.; Springer: Berlin/Heidelberg, Germany, 2006; pp. 371–427, ISBN 978-3-540-32144-6.
89. Horn, D.R.; Horn, B.M.; Delach, M.N. Distribution of Ferromanganese Deposits in the World Ocean. In *Ferromanganese Deposits on the Ocean Floor*; Horn, D.R., Ed.; The Office for the International Decade of Ocean Exploration, National Science Foundation: Alexandria, VA, USA, 1972; pp. 9–18.
90. Vlasova, I.E.; Kuptsov, V.M. New Data on the Growth Rates of Iron and Manganese Concretions in the Southeast Pacific Ocean. *Oceanology* **1994**, *34*, 113–120.
91. Goodell, H.G. *USNS Eltanin Marine Geology Cruises 16 to 27*; Florida State University Sedimentological Research Library: Tallahassee, FL, USA, 1968.
92. Elt24_016_016_013.Jpg. (2002 × 1367). Available online: https://www.ngdc.noaa.gov/mgg/curator/data/eltanin/elt24/seabed_photos/elt24_016_016_013.jpg (accessed on 26 October 2024).
93. Rea, D.K.; Leinen, M. Crustal Subsidence and Calcite Deposition in the South Pacific Ocean. *Initial. Rep. Deep. Sea Drill. Proj.* **1986**, *92*, 299–303.
94. Bureau of Ocean Energy Management. *Investigation of an Historic Seabed Mining Site on the Blake Plateau*; Bureau of Ocean Energy Management: Washington, DC, USA, 2019.
95. Pratt, R.M.; McFarlin, P.F. Manganese Pavements on the Blake Plateau. *Science* **1966**, *151*, 1080–1082. [CrossRef]

96. White, M.P.; Farrington, S.; Galvez, K.; Hoy, S.; Newman, M.; Rabenold, C. *OER Cruise Report 19-07: EX-19-07, Southeastern U.S. Deep-Sea Exploration (Mapping & ROV)*; Office of Ocean Exploration and Research, Office of Oceanic and Atmospheric Research, NOAA: Silver Spring, MD, USA, 2019; p. 46.
97. Gonzalez, F.J.; Somoza, L.; Hein, J.R.; Medialdea, T.; Leon, R.; Urgorri, V.; Reyes, J.; Martin-Rubi, J.A. Phosphorites, Co-Rich Mn Nodules, and Fe-Mn Crusts from Galicia Bank, NE Atlantic: Reflections of Cenozoic Tectonics and Paleoceanography. *Geochem. Geophys. Geosyst.* **2016**, *17*, 346–374. [[CrossRef](#)]
98. Xavier, A. Ferromanganese Deposits off Northeast Brazil (S. Atlantic). *Mar. Geol.* **1982**, *47*, 87–99. [[CrossRef](#)]
99. Guan, Y.; Sun, X.; Ren, Y.; Jiang, X. Mineralogy, Geochemistry and Genesis of the Polymetallic Crusts and Nodules from the South China Sea. *Ore Geol. Rev.* **2017**, *89*, 206–227. [[CrossRef](#)]
100. Cronan, D.S. Deep-Sea Mining: Historical Perspectives. In *Perspectives on Deep-Sea Mining: Sustainability, Technology, Environmental Policy and Management*; Sharma, R., Ed.; Springer International Publishing: Cham, Switzerland, 2022; pp. 3–11, ISBN 978-3-030-87982-2.
101. Cronan, D.S. Chapter 2 Deep-Sea Nodules: Distribution and Geochemistry. In *Elsevier Oceanography Series*; Glasby, G.P., Ed.; Elsevier: Amsterdam, The Netherlands, 1977; Volume 15, pp. 11–44, ISBN 0422-9894.
102. Lutz, M.J.; Caldeira, K.; Dunbar, R.B.; Behrenfeld, M.J. Seasonal Rhythms of Net Primary Production and Particulate Organic Carbon Flux to Depth Describe the Efficiency of Biological Pump in the Global Ocean. *J. Geophys. Res.* **2007**, *112*. [[CrossRef](#)]
103. Suess, E. Particulate Organic Carbon Flux in the Oceans—Surface Productivity and Oxygen Utilization. *Nature* **1980**, *288*, 260–263. [[CrossRef](#)]
104. Straume, E.O.; Gaina, C.; Medvedev, S.; Hochmuth, K.; Gohl, K.; Whittaker, J.M.; Fattah, R.A.; Doornenbal, J.C.; Hopper, J.R. GlobSed: Updated Total Sediment Thickness in the World’s Oceans. *Geochem. Geophys. Geosyst.* **2019**, *20*, 1756–1772. [[CrossRef](#)]
105. Naar, D.F. (College of Marine Science, University of South Florida, Tampa, FL, USA). Personal communication, 2021.
106. Caress, D.W.; Chayes, D.N. Improved Processing of Hydrosweep DS Multibeam Data on the R/V Maurice Ewing. *Mar. Geophys. Res.* **1996**, *18*, 631–650. [[CrossRef](#)]
107. Caress, D.W.; dos Santos Ferreira, C.; Chayes, D.N. MB-System (Version 5.8.1) [Computer Software]. Available online: <https://github.com/dwcaress/MB-System/releases/tag/5.8.1> (accessed on 22 March 2024).
108. Mussett, M.; Kaufmann, M.; Smit, H.; McIntyre, J. Conrad Supplementing Resource Estimation with Domain Establishment from Trained Remote Sensing Acoustics. In *UMC 2024 Abstract Booklet, Rarotonga*; IMMS: Rarotonga, Cook Islands, 2024.
109. Haar, C.; Misiuk, B.; Gazzola, V.; Wells, M.; Brown, C.J. Harmonizing Multi-Source Backscatter Data Using Bulk Shift Approaches to Generate Regional Seabed Maps: Bay of Fundy, Canada. *J. Maps* **2023**, *19*, 2223629. [[CrossRef](#)]
110. Hagen, R.A.; Baker, N.A.; Naar, D.F.; Hey, R.N. A SeaMARC II Survey of Recent Submarine Volcanism near Easter Island. *Mar. Geophys. Res.* **1990**, *12*, 297–315. [[CrossRef](#)]
111. United Nations. Kunming-Montreal Global Biodiversity Framework. In Proceedings of the Fifteenth Meeting of the Conference of the Parties to the Convention on Biological Diversity (Part Two) Decision 15/4, Montreal, BC, Canada, 7–19 December 2022.
112. United Nations. Nations Adopt Four Goals, 23 Targets for 2030 in Landmark UN Biodiversity Agreement. In Proceedings of the Convention on Biological Diversity December, Montreal, BC, Canada, 7–19 December 2022.
113. Convention on Biological Diversity. *Kunming-Montreal Global Biodiversity Framework Draft Decision Submitted by the President*; Convention on Biological Diversity: Montreal, BC, Canada, 2022.
114. United Nations. *United Nations Convention on the Law of the Sea*; United Nations: New York, NY, USA, 1982.
115. Mayer, L.; Jakobsson, M.; Allen, G.; Dorschel, B.; Falconer, R.; Ferrini, V.; Lamarche, G.; Snaith, H.; Weatherall, P. The Nippon Foundation—GEBCO Seabed 2030 Project: The Quest to See the World’s Oceans Completely Mapped by 2030. *Geosciences* **2018**, *8*, 63. [[CrossRef](#)]
116. The Nippon Foundation-GEBCO Seabed 2030 Project Announces New Global Initiatives in Pursuit of Mapping Entire Ocean Floor—All About Shipping. Available online: <https://allaboutshipping.co.uk/2019/10/22/the-nippon-foundation-gebco-seabed-2030-project-announces-new-global-initiatives-in-pursuit-of-mapping-entire-ocean-floor/> (accessed on 26 October 2024).
117. Thorsnes, T.; Bjarnadóttir, L.R.; Jarna, A.; Baeten, N.; Scott, G.; Guinan, J.; Monteys, X.; Dove, D.; Green, S.; Gafeira, J.; et al. National Programmes: Geomorphological Mapping at Multiple Scales for Multiple Purposes. In *Submarine Geomorphology*; Micallef, A., Krastel, S., Savini, A., Eds.; Springer International Publishing: Cham, Switzerland, 2018; pp. 535–552, ISBN 978-3-319-57852-1.
118. Integrated Ocean & Coastal Mapping. Available online: <https://iocm.noaa.gov/seabed-2030.html> (accessed on 26 October 2024).
119. NLA International. *SEABED 2030—Wind in the Sails Phase 1 Objective 1*; The Nippon Foundation-GEBCO: Tokyo, Japan, 2020.

Disclaimer/Publisher’s Note: The statements, opinions and data contained in all publications are solely those of the individual author(s) and contributor(s) and not of MDPI and/or the editor(s). MDPI and/or the editor(s) disclaim responsibility for any injury to people or property resulting from any ideas, methods, instructions or products referred to in the content.